



HAL
open science

Tectonics of Cerberus Fossae unveiled by marsquakes

Simon C. Stähler, Anna Mittelholz, Clément Perrin, Taichi Kawamura,
Doyeon Kim, Martin Knapmeyer, Géraldine Zenhäusern, John Clinton,
Domenico Giardini, Philippe Lognonné, et al.

► **To cite this version:**

Simon C. Stähler, Anna Mittelholz, Clément Perrin, Taichi Kawamura, Doyeon Kim, et al.. Tectonics of Cerberus Fossae unveiled by marsquakes. *Nature Astronomy*, 2022, 10.1038/s41550-022-01803-y . insu-03868823

HAL Id: insu-03868823

<https://insu.hal.science/insu-03868823v1>

Submitted on 14 Mar 2023

HAL is a multi-disciplinary open access archive for the deposit and dissemination of scientific research documents, whether they are published or not. The documents may come from teaching and research institutions in France or abroad, or from public or private research centers.

L'archive ouverte pluridisciplinaire **HAL**, est destinée au dépôt et à la diffusion de documents scientifiques de niveau recherche, publiés ou non, émanant des établissements d'enseignement et de recherche français ou étrangers, des laboratoires publics ou privés.

TECTONICS OF CERBERUS FOSSAE UNVEILED BY MARSQUAKES

A PREPRINT

 **Simon C. Stähler**
Institute for Geophysics
ETH Zürich

 **Anna Mittelholz**
Department of Earth and Planetary Sciences
Harvard University

 **Clément Perrin**
LPG-OSUNA
Nantes Université

 **Taichi Kawamura**
Université Paris Cité
Institut de physique du globe de Paris, CNRS
Paris, France

 **Doyeon Kim**
Institute for Geophysics
ETH Zürich

 **Martin Knapmeyer**
Institute for Planetary Science
DLR Berlin

 **Géraldine Zenhäusern**
Institute for Geophysics
ETH Zürich

 **John Clinton**
Institute for Geophysics
ETH Zürich

 **Domenico Giardini**
Institute for Geophysics
ETH Zürich

 **Philippe Lognonné**
Université Paris Cité
Institut de physique du globe de Paris, CNRS

 **W. Bruce Banerdt**
Jet Propulsion Laboratory
California Institute of Technology

June 28, 2022

1 **Keywords** Mars | Tectonics | Volcanism | Marsquakes

ABSTRACT

2 The InSight mission has measured Mars' seismicity since February 2018 and has allowed to investigate
3 tectonics on another planet. Seismic data shows that most of the widely distributed surface faults are
4 not seismically active, and that seismicity is mostly originating from a single graben structure, the
5 Cerberus Fossae. We show that both major families of marsquakes characterized by low and high
6 frequency content, LF and HF events respectively, are located on central and eastern parts of this
7 graben system. LF hypocenters are located at 15-50 km depth and the spectral character suggests a
8 structurally weak, potentially warm source region consistent with recent volcanic activity at those
9 depths. HF marsquakes occur in the brittle, shallow part of the crust and might originate in fault
10 planes associated with the graben flanks. Estimated magnitudes are between 2.8 and 3.8, resulting in
11 a total seismic moment release within Cerberus Fossae of $1.4\text{-}5.6 \times 10^{15}$ Nm/yr, or at least half of the
12 observed value of the entire planet. Our findings confirm that Cerberus Fossae represents a unique
13 tectonic setting shaped by current day volcanic processes, with implications for minimum local heat
14 flow.

15 Introduction

16 Faults are widespread and common on the martian surface [1, 2], providing evidence for brittle deformation throughout
17 the planet's history. Due to the lack of recent widespread volcanism, plate tectonics or high erosion rates which recycle
18 the surfaces of Venus or Earth, martian faults are well preserved over billions of years and do not necessarily correlate
19 with recent tectonic deformation. The InSight mission landed on Mars to observe current day seismicity and thus
20 tectonic activity using a broadband seismometer [3, 4]. Around InSight's landing site [5], wrinkle ridges and lobate
21 scarps, interpreted as buried reverse faults resulting from compression, are widely spread, with clusters in the large
22 Isidis and Hellas impact basins, but also in the planes of Hesperia, Arcadia and Amazonis (Figure 1). Their abundance

was interpreted as the result of secular cooling and associated shrinking of the planet [6], in combination with the weight of the large Tharsis volcanic region 6000 km to the East [7]. Young (<600 Ma), extensional tectonic structures are oriented radial to Tharsis (Figure 13). Westward, these are Cerberus Fossae [8] in Eastern Elysium Planitia, and further southward these are Memnonia and Sirenum Fossae [9]. In conclusion, based on the distribution of young faults one might expect widespread seismic activity north and south-east of the InSight landing site. However, the first seismic data revealed a different picture.

The most significant marsquakes during InSight's first Martian year of operations (observed on Sols 173 and 235 of the mission, thus named *S0173a* and *S0235b*) were located at the approximate distance and in direction of Cerberus Fossae [10, 11]. Analysis of seismic waveforms showed that source mechanisms of the large events from Sols 173 and 235 are consistent with an extensional setting [12], suggestive of ongoing opening of the Cerberus Fossae. Until Sol 1100 (2021/12/31), 18 out of 24 low-frequency (LF) marsquakes for which a location could be determined, have been located at a distance consistent with Cerberus Fossae [13, 14] and for seven of those, a focal mechanism could be determined, generally extensional [15]. LF quakes are similar in character to earthquakes, with clear P- and S-waves, and they are thought to occur in the lower crust or uppermost mantle [11], between 15 and 50 km depth [12, 16]. A second class of marsquakes is termed high-frequency (HF) events, due to significant signal energy above 2 Hz [13]. A long signal duration is interpreted as the result of a shallow hypocenter of less than a few km depth, which excites reverberations of seismic waves in shallow subsurface layers [17]. HF events have been detected in much larger numbers, 1150 until 2021/12/31, yet they have smaller magnitudes than LF events; their distance is clustered around 1500 km, and due to a lack of clear polarisation, their direction as seen from the lander has not been determined. Thus no tectonic explanation has been provided for this most common type of Martian seismicity yet. Here, we determine the direction of HF events and corroborate the unique tectonic setting of the Cerberus Fossae System. We investigate the source character of LF events which indicate a warm source region at depth as opposed to the brittle and shallow source region of HF events. Combining all information from both event classes allows to derive a consistent picture of the tectonics in the Cerberus Fossae system.

So far, no other tectonic feature on the InSight hemisphere of Mars has been unequivocally confirmed to be seismically active [13], and only recently, on Sol 976 (2021/09/01), InSight detected large marsquakes on the far side, in the Southern Tharsis province [18]. Since no marsquakes at all have been clearly localized on wrinkle ridges or lobate scarps, i.e. contractional features, Cerberus Fossae offers unique insight into Mars' tectonics as a whole.

Geological context

The Cerberus Fossae system is approximately 1200-2300 km (20-40°) east of the InSight lander (Figure 2b,c). It has been described as a dike-induced graben system [19], or a system of collapsed and widened volcanic fissures [20, 21]; we will refer to it as a system of fossae, which is the descriptive term for elongated fractures on Mars. Cerberus Fossae consists of five main graben features (G1-G5 in Figure 2b) trending NW to SE and between 250 and 600 km long, but further segmented. Smallest segments that can be identified on the surface are 5-10 km long [19]. The westernmost fossae are more mature (i.e., larger width and throw) and well connected, as opposed to the hardly connected segments at the eastern fossae [19]. Cerberus Fossae was previously identified as the location with most recent volcanic activity on Mars [2] dated to less than 10 Ma [22], contemporary with the deposition of surficial basalt deposits over Eastern Elysium Planitia [8, 23]. Moreover, [24] identified symmetric dust deposits in the central part of the fossae, the Cerberus Mantling Unit (CMU; Figure 2d), and hypothesized that those are pyroclastic deposits younger than 200 ka. Large-scale radially extensional and concentric contractional faulting (global fault map in Figure 13) from the topographic load of the Tharsis volcanic province would create the extensional stress field in North-west direction in Eastern Elysium Planitia [7, 25]. The actual fracturing in the specific location could be due to weakening of the crust due to partial melting below Elysium Mons and a dike system extending from there [26, 27].

Marsquake Hypocenter Locations

Figure 1 shows the combined probability density of all LF quake locations including distance and direction using recently obtained back azimuth estimates [28] and velocity models [29], and it peaks at Cerberus Fossae. The uncertainty on back-azimuth results in a relatively large geographical spread in North-South direction. But given that the distance spread (in East-West direction) of the observed marsquake cluster is small, it can a priori be assumed that their N/S spread is of similar magnitude, allowing to place all of these events into Cerberus Fossae. The five segments of the Cerberus Fossae grabens (G1-G5) are concentrated in two main regions [19], where G1, G2, G3 are in a distance range of 18° – 27° from InSight, while G4 spans the range of 33° – 39°. G5 is more faint, less mature and bridges the two main regions. The graben strike is 15° off the direction of the lander. Distance differences of LF events can most easily be explained by different locations along the fossae. To identify such locations, we evaluate if the event cluster is

76 consistent with certain locations along the fossae (Figure 2a,b) when varying the seismic velocity models. In the "near"
 77 end-member model, the cluster of events would occur at the eastern end of G1 or in G5. In the "far" case, it would be
 78 placed on G5 and G4. In any case, the dominant location of marsquakes at the eastern end of the western section is
 79 compatible with the observation of east-ward decreasing maturity, that would imply increased stress concentrations
 80 at the propagating fossae [19]. A single event, S0325a [13] would be located at the eastern end of G4 (not shown in
 81 Figure 1), but given that this event has a poorly determined back azimuth [28], it cannot be clearly attributed to Cerberus
 82 Fossae. We conclude that the majority of *localized* LF events on the InSight hemisphere cluster in central Cerberus
 83 Fossae (Figure 1).

84 Localising HF events has not been attempted at all so far due to the strong scattering and the lack of ballistic arrivals
 85 [17]. We realign the events to better constrain relative distances and stack horizontal component envelopes. We find a
 86 surplus of energy in $78 \pm 12^\circ$ backazimuth around the P-wave arrival, consistent with a source in direction of Cerberus
 87 Fossae (see Supplement). We further examine their distance distribution and while it is broader c.f. LF events, we find
 88 that it indeed matches the extent of Cerberus Fossae (Figure 1 and 2a). Thus, we can plausibly assume that shallow HF
 89 seismicity also originates in Cerberus Fossae. The HF sources are spread over a large part of the Fossae, as opposed to
 90 the more focused distribution of deeper LF events.

91 Seismic Moment

92 Estimating Seismic Moment Release

93 MQS routinely estimates magnitudes [30] and their uncertainties. For LF events, the magnitude uncertainty takes into
 94 account the distance uncertainty as well as the error in estimating the long-period amplitude [30]. Identification of
 95 marsquakes is limited to times of low wind at InSight, which make up approximately one third of the total duration
 96 averaged over the mission [13, 31]. When estimating the total seismic activity rate of a region, one needs to take into
 97 account not only the detection probability due to wind noise, but also the inherent randomness of number of events
 98 per year. [32] propose a Markov Chain Monte Carlo method to estimate the likelihood for annual moment release and
 99 maximum event size, given a short and incomplete catalog. Following this procedure, we estimate the total annual
 100 moment rate in Cerberus Fossae as $1.4\text{-}5.6 \times 10^{15}$ Nm/yr (SM A.3). Regarding Mars' seismicity as a whole, SEIS
 101 observed a total of 39 LF marsquakes on the InSight hemisphere rated as quality A,B or C (A-D is highest to lowest,
 102 where D is unlocatable) by MQS up to December 31, 2021 [14]. Five of them are unequivocally located outside
 103 Cerberus Fossae, compared to 14 in Cerberus Fossae. The remaining 20 cannot be located due to noise. Thus, from the
 104 observations so far, the small region of central Cerberus Fossae accounts for at least half of the seismic moment release
 105 of the whole InSight hemisphere.

106 Seismic vs Geological Deformation

107 Following the morphological estimate of [22], the formation of the Cerberus Fossae grabens G1-G4 requires deformation
 108 equivalent to a seismic moment, $M_{0,\text{total}} = 2.1 \pm 0.5 \times 10^{24}$ Nm, assuming a constant rate \dot{M}_0 since initiation of the
 109 spreading 5-20 Ma ago, $\dot{M}_0 = 0.5 - 2.2 \times 10^{17}$ Nm/yr. This prediction exceeds our seismic observation by a factor of
 110 50 and is a first indication that the current seismicity rate is not representative for the entire formation process.

111 Next, we focus on the observed seismicity cluster which spreads over 400 km distance and a range of ~ 20 km in depth
 112 (thus providing an area A). Using a shear modulus of $\mu = 24$ GPa [33] and assuming that all of the seismicity was
 113 extensional, the observation is equivalent to a slip rate of $\dot{s}_{\text{seism}} = \frac{\dot{M}_0}{\mu A} = 7 - 30 \times 10^{-6}$ m/yr. For G1 and G2, the
 114 geological deformation rate is $\dot{d}_{\text{geol}} = 5 - 73 \times 10^{-5}$ m/yr [34]. The central young CMU (53-210 ka [24]) shows a
 115 throw of at least 100 m, equivalent to a slip rate of $\dot{s}_{\text{geol}} = 5 - 20 \times 10^{-4}$ m/yr over the last few 10 ka. We therefore
 116 conclude that the current seismic slip rate \dot{s}_{seism} explains only 1 - 10% of the total deformation, d_{geol} , preserved in the
 117 geological record.

118 The shallow seismicity associated with the HF events is at least a factor of 10 below the LF events due to their smaller
 119 magnitudes and it is distributed over a larger area. It can therefore not explain the discrepancy between geological
 120 deformation and observed seismicity.

121 A Case for Dike-induced Tectonic Activity in the Source Region

122 Spectral Characteristics

123 The duration of a quake, whether on Earth or Mars, places a limit on the coherent high-frequency seismic energy radiated
 124 from it. This is typically expressed via the corner frequency in the source spectrum, f_c , above which displacement
 125 amplitude, $A(f)$, decreases as f^n , where $2 < n < 3$ [35]. For all investigated LF events in Cerberus Fossae, we find
 126 that $0.45 < f_c < 0.95$ Hz. As shown in Figure 4c, this is significantly less than the values found empirically for
 127 $M_W \approx 3$ earthquakes [36, 37], which is 2-10 Hz. In comparison, LF marsquakes outside Cerberus Fossae, specifically a
 128 recent marsquake in Syrtis Major Planum, S1102a (2022/01/02, Fig 4b), but also other events at distances of 3000-4000
 129 km (red stars in Fig 4c) show significantly higher values of $f_c > 1.5$ Hz. The corner frequency of the shallow HF events
 130 is significantly higher (see figure 4b). For the largest HF events, a roll-off in displacement spectrum is observed above 3
 131 Hz, which puts a lower limit on the f_c , given the unknown attenuation of the upper crust. While their magnitudes range
 132 from $1.5 < M_W < 2.5$, this f_c is still at the low end of terrestrial quakes, although it must be noted that their absolute
 133 magnitude is uncertain due to the complicated propagation mechanism.

134 A feasible explanation for the observation of "slow" quakes is a significantly reduced shear wave velocity, β , in the
 135 source region, because in classic models f_c scales linearly with β [35], i.e.,

$$f_c \propto \beta \sqrt[3]{\Delta\sigma/M_0} \quad (1)$$

136 where $\Delta\sigma$ is the stress drop. InSight observed low β of 1.3-1.8 km/s in the uppermost ten km below the lander as
 137 derived using receiver functions [10, 33] and autocorrelations [38], which is a factor of ~ 2 below the value in terrestrial
 138 crustal models [e.g. 39]. If the hypocenters were located within this layer, this could explain a factor of 2 in corner
 139 frequency compared to the bulk of terrestrial crustal earthquakes, but hardly the observed 5-10. Also, so far all published
 140 results agree on LF event depths of at least 15 km [12, 16, 40, 41], where β is comparable to terrestrial values.

141 Local weakening, e.g. due to warmer materials nearby a dike in the source region, could present a second effect leading
 142 to the observations. The stress drop ($\Delta\sigma$ in eq. 1) describes the difference of the shear stress on the fault plane before
 143 and after the quake. It can be derived analytically for simple fault geometries in homogeneous media, and otherwise
 144 represents an empirical term [42]. As a general rule, low values for f_c and thus $\Delta\sigma$ are found in volcanic settings,
 145 where material is heated and close to ductile behaviour [43]. This would require the hypocenters to be located in a zone
 146 of increased temperature, possibly close to a magma chamber feeding shallower dikes (Figure 5). This explanation is
 147 consistent with the depth estimates for LF and HF events. The deep LF events are closer to the weakening heat sources
 148 and thus show a slower rupture process than the more shallow and fast, brittle HF events.

149 A third possible explanation would be that the lower gravity on Mars will reduce yield strength and could thus lead to
 150 generally lower stress drops and therefore f_c . However, this general trend is not seen on Earth, e.g. when comparing
 151 earthquakes at different depths [44], and shallow moonquakes show even higher f_c values [45]. Finally, as stated above,
 152 large marsquakes outside of Cerberus Fossae have significantly higher corner frequencies, which fall within the range
 153 expected for terrestrial quakes of similar size (red line in Figure 4b). This observation confirms that Cerberus Fossae
 154 events are different and, combined with the very frequent and localized observations of quakes from this source region,
 155 highlights the unique setting of Cerberus Fossae.

156 Recent Volcanism in Cerberus Fossae

157 The CMU near Zunil crater has been hypothesized as a recent product of explosive volcanism [24], based on the
 158 symmetric distribution of dust and streaking of secondary craters away from the structure (Figure 2d). The dust and
 159 streaking directions overlay that of Zunil crater itself, dated at 0.1-1 Ma. While the hypothesis of explosive volcanism
 160 may be unproven, the detailed age estimates of the CMU of 53-210 ka, make it one of the youngest features mapped on
 161 the Martian surface to date [24]. Because there is no sign of younger volcanism locally, the structure would have to be
 162 considered dormant or inactive.

163 Terrestrial volcanoes of this age can still be in an active state with ongoing fluid motion identified by seismic activity
 164 [46]. The observation of marsquakes around the CMU is thus intriguing and we compare our observations with two
 165 categories of seismic activity near dormant volcanoes on Earth (for an overview, see e.g. [47]): (1) Deep low frequency
 166 events (DLEs), which are "slow" quakes of magnitudes < 2 . These events typically occur in swarms, i.e. week- to
 167 year-long activity bursts. (2) Volcanic tremor, long-duration, monochromatic signals.

168 In comparison, our studied events on Mars do not quite match any of these two categories. While martian LF events
 169 are abnormally slow, they do not qualify as DLEs, because they are too large in magnitude (which would require
 170 very significant subsurface magma motion). Moreover, their recurrence rate also shows no deviation from a stationary
 171 Poisson process (SM A.3), unlike DLEs, which occur in swarms. We note that at distances of 1500 km or more, the

172 VBB seismometer lacks the resolution to observe very slow events, including DLEs below magnitude 2.5 (region below
 173 the red line in Figure 4). We therefore cannot rule out signals from fluid motion, but discussed event observations are
 174 not consistent with Earth-like DLEs. Others [48] investigated whether several LF marsquakes could be explained by
 175 volcanic tremor, but found that for the magnitude and spectral content, very large magma flow rates over short time
 176 windows would be needed. This is in apparent contradiction to the low number of marsquakes observed so far and the
 177 lack of surficial expressions of current active volcanism. Also, the events discussed in this study show very clear P- and
 178 S-arrivals, unlike the more emergent signals of tremor on Earth. In summary, we do not find evidence of tremor or
 179 generally fluid motion in the seismic data.

180 **Inferred Rupture Size**

181 Lastly, under the assumption of a circular source, f_c allows to infer the source radius as $r = 0.38 \frac{\beta}{f_c}$ [49]. Within
 182 the range of β between 2-3 km/s, we obtain rupture plane radii of 1200–1800 m. This is below the minimum size
 183 of mapped surface segments within the Cerberus Fossae grabens (5-10 km [19]), suggesting that small to moderate
 184 size marsquakes are not primarily limited by fracture geometry and that over longer observation times, significantly
 185 larger marsquakes occur, compatible with the large, potentially co-seismic boulder avalanche traces observed in orbital
 186 imaging [50]. The shallower HF quakes likely happen in the uppermost, low- β layer [33], with source radii between
 187 150 and 300 m.

188 **Discussion: The Evolution of Cerberus Fossae**

189 Seismic data confirm ongoing opening of the Cerberus Fossae on Mars. Seismicity at 15-50 km depth with slow rupture
 190 processes suggests an extensional stress regime located in a warm source region. If the seismicity of the central event
 191 cluster is related to the CMU, the observed seismic strain rate is far too low for a constant, slow opening of the fractures.
 192 This is consistent with rapid creation in a volcanic eruption 53-210 ka ago, as observed for dike-induced fractures on
 193 Earth [51].

194 The east-west distribution of our events shows focused seismic activity in the center of Cerberus Fossae with generally
 195 low current seismicity compared to inferences from the geological record. This indicates that the opening rate of the
 196 grabens has not been constant. Instead, most of them likely opened rapidly and became mostly passive after a short
 197 time. The seismic observation period is short and our data merely represent a snapshot of the overall seismicity of
 198 Cerberus Fossae. Nevertheless, the fact that we do not see LF seismicity in most parts of Cerberus Fossae, specifically
 199 in the fractured western part where the largest deformation can be found, suggests a dynamic process that ceases after
 200 an initially active phase and continues to propagate eastward.

201 We propose that the shallow seismicity from HF events is created by ruptures at shallow depth due to the graben
 202 structure itself, possibly the subsurface continuation of the graben flanks (Figure 5). The rapid rupture associated with
 203 these quakes is not consistent with sources such as landslides or other mass wasting processes. More likely it is caused
 204 by the release of residual stress. A modulation of the HF quake rate with a period of one Martian year was found [31]
 205 and its phase matches the peak solar elevation in equatorial latitudes. Given that significant parts of Cerberus Fossae are
 206 deep enough to be in shadow over half of a Martian year, this is a plausible correlation and consistent with shallow
 207 sources. However, a physical model connecting the two factors, illumination and quake rate, is still missing.

208 Globally, the clearly localized seismicity suggests that global contraction and therefore lithospheric compression are
 209 not the dominant driver of contemporary tectonics on Mars. Cerberus Fossae alone releases $1.4\text{-}5.6 \times 10^{15}$ Nm/yr
 210 seismic moment, a factor of 2-8 more than the Moon globally [32], where shallow seismicity has been identified on
 211 compressional faults [52]. The slow character of the Cerberus Fossae events requires a warm source region. To be
 212 close to ductile rheology, a temperature of 1000 ± 100 K is required for basaltic compositions [53, 54]. Assuming a
 213 quake depth of 40 ± 10 km, this results in a local crustal thermal gradient $\Delta T/\Delta z = 20 \pm 2$ K/km in Cerberus Fossae
 214 and a local heat flow of 36 ± 10 mW/m² (assuming thermal properties of basalt [55]), a factor of 1.7 above the global
 215 average values of 21 ± 7 mW/m² and 22 ± 1 mW/m² found by joint seismic and geophysical inversions [41, 56]. Such
 216 a localized high heat flow in Elysium has strong geodynamical implications for the crustal thickness of the whole planet,
 217 namely, it is difficult to reconcile with a thicker crust in the Southern hemisphere [27].

218 The distribution and character of marsquakes show that the global stress field cannot exclusively explain the origin
 219 of Cerberus Fossae. Instead, partial melting below Elysium likely weakens the crust locally and allows the grabens
 220 of Cerberus Fossae to open. Across the solar system, a pattern emerges, where the present-day tectonics of the larger
 221 terrestrial planets - Mars, Venus, and the Earth - is dominated by internal dynamics [57] instead of purely passive
 222 cooling and shrinking, as it is found on the smaller Moon and Mercury.

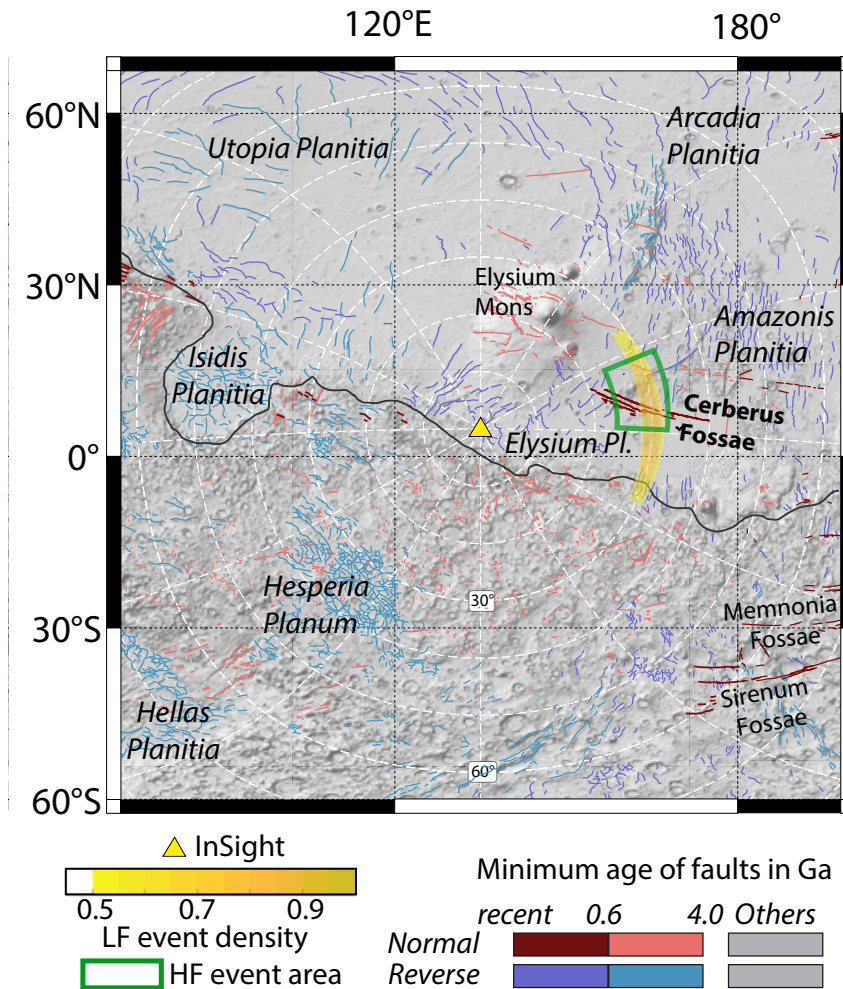


Figure 1: Faults and major geographic features around the InSight landing site [1, 19] color-coded by age. The yellow shaded area marks the normalized density of low frequency (LF) quakes [14, 28]. The green box highlights the backazimuth range found by our analysis for HF marsquakes, corresponding to the dashed line in figure 3 and the distance range in which 80% of seismicity is present. Background shading: MOLA topographic map [58]. A global version of this map is available in the supplement (fig. 13)

223 Acknowledgements

224 We acknowledge NASA, CNES, partner agencies and institutions (UKSA, SSO, DLR, JPL, IPGP-CNRS, ETHZ, IC,
 225 and MPS-MPG), and the operators of JPL, SISMOC, MSDS, IRIS-DMC, and PDS for providing SEED SEIS data.
 226 S.C.S. acknowledges funding from ETH research grant ETH-10 17-3. S.C.S., G.Z., and D.G. acknowledge support
 227 from ETHZ through the ETH+ funding scheme (ETH+2 19-1: “Planet MARS”). A.M. acknowledges support from
 228 ETH 19-2 FEL-34 and the Harvard Daly Postdoctoral Fellowship. C.P. acknowledges support from CNES as well as
 229 Agence Nationale de la Recherche (ANR-14-CE36-0012-02 and ANR-19-CE31-0008-08). W.B.B. was supported by
 230 the NASA InSight mission and funds from the Jet Propulsion Laboratory, California Institute of Technology, under a
 231 contract with the National Aeronautics and Space Administration (80NM0018D0004). This is InSight contribution 233.

232 1 Tables

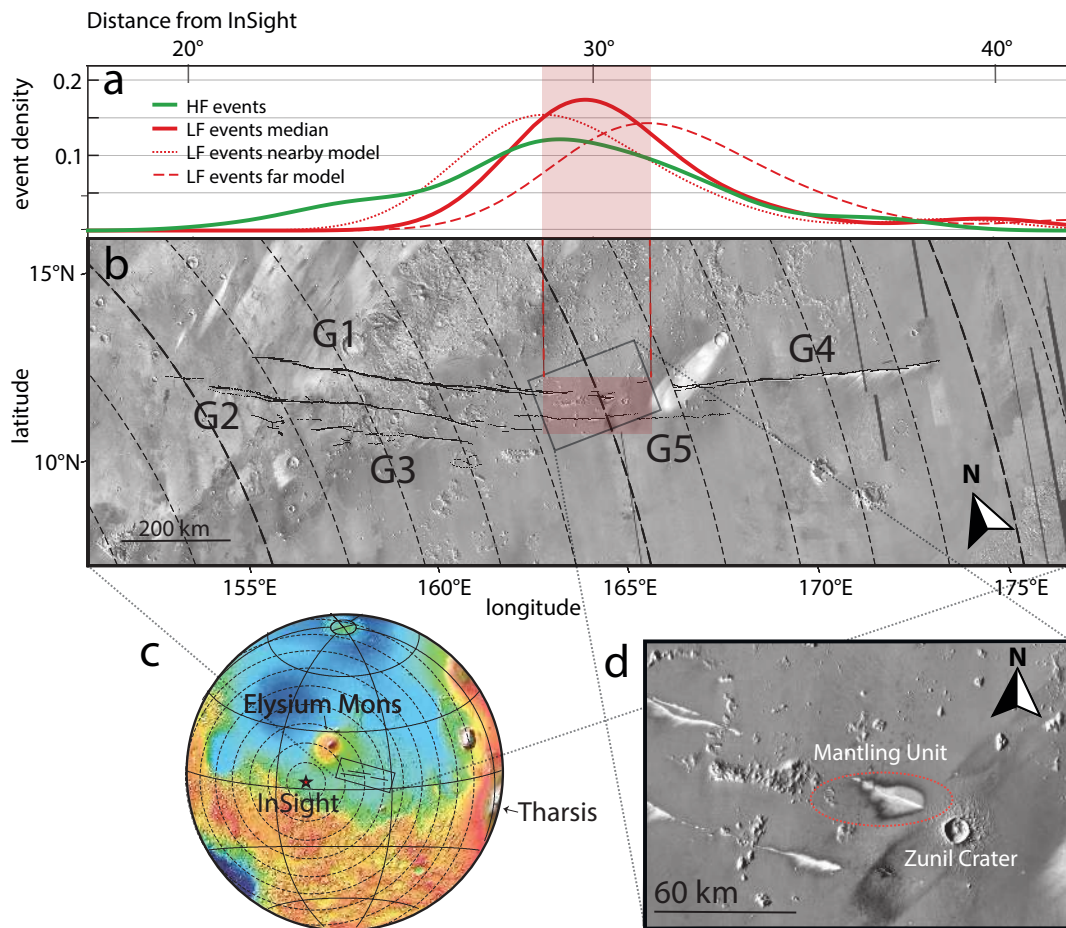


Figure 2: (a) Density of seismic moment release along the profile of Cerberus Fossae. Probability density functions (PDF) from a Gaussian kernel density estimation of high frequency (HF; green) and low frequency (LF; red) moment are shown separately. For the LF events, 3 candidate distributions based on different mantle models are shown ("median" model is shown in Figure 1). The red box highlights the area between near and far model peaks in (a) for easier comparison with (b). (b) Oblique Mercator projection of Mars Odyssey's Thermal Emission Imaging System (THEMIS; day-time infrared) highlighting the 5 main graben features G1-G5 of Cerberus Fossae (mapping from [19]). (c) MOLA topography inset for global context and 10 degree distance circles around InSight. (d) The area of highest marsquake density: The Cerberus Mantling unit recently identified as a volcanically active feature by [24] is circled.

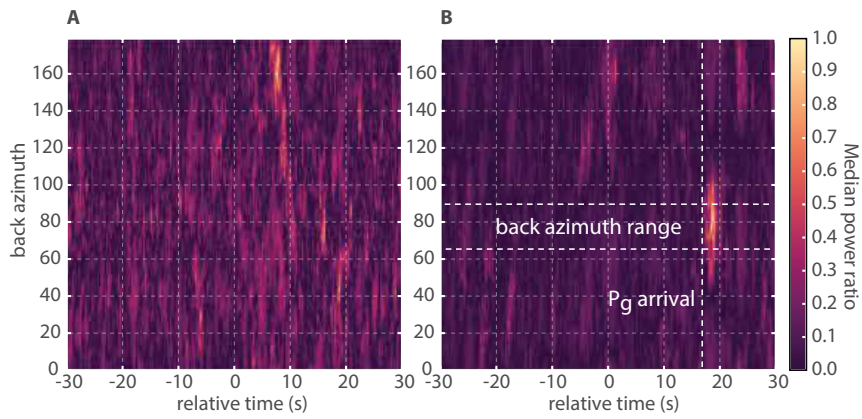


Figure 3: Energy ratio between radial and transversal horizontal component for HF envelope stack (a) before and (b) after re-alignment (see A.2). The energy maximum at a backazimuth of $78 \pm 12^\circ$ (dashed lines) corresponds to P-wave energy from the central part of Cerberus Fossae. The time axis is relative to an arbitrary offset used before alignment, the P_g -arrival is thus marked.

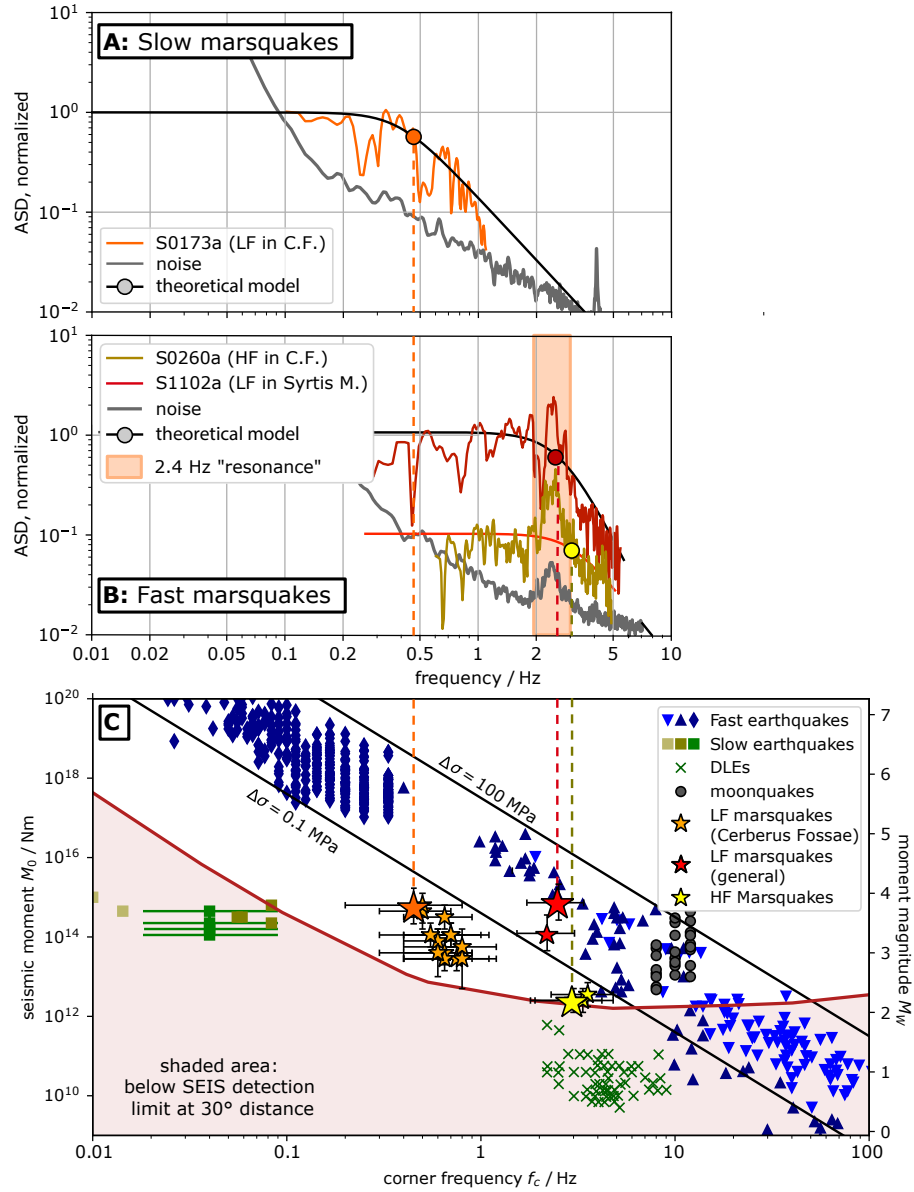


Figure 4: Spectra of marsquakes and source parameters compared to terrestrial and lunar quakes. (A): Source spectra of Cerberus Fossae low frequency (LF) marsquakes S0173a. (B): Source spectrum for high frequency (HF) marsquake S0260a and distant LF marsquake S1102a. The source spectra were estimated from the vertical component for the P-wave window, normalized and corrected for attenuation, assuming $Q_\mu = 1000$, to match P- and S-falloff. The black solid lines show best fitting theoretical source spectra using a Brune model with exponent $n = 2$ or 3 , circles are modelled corner frequencies. The background noise curves in (A) and (B) are from data before the P-wave arrival. The orange area in (B) is the local "2.4 Hz" subsurface resonance described in [59, 60]. (C): Seismic moment M_0 vs corner frequency f_c for different types of quakes observed on the Earth, the Moon and Mars. Blue symbols mark regular, "fast" earthquakes, following a cube law between the seismic moment and corner frequency for 3 datasets of shallow earthquakes (in order of symbols: [36, 61, 62]). The brown squares mark a group of deep, slow events in Japan [63], the green crosses mark slow events related to volcanism, observed in Germany [46]; gray dots are fast shallow moonquakes [45]. Black lines are f_c values for stress drops of 0.1 and 100 MPa for $\beta = 3$ km/s. HF marsquakes (yellow stars), as well as LF marsquakes outside Cerberus Fossae (red star) follow the $f_c \propto M^{-3}$ trend of earthquakes, while Cerberus Fossae LF events are significantly slower.

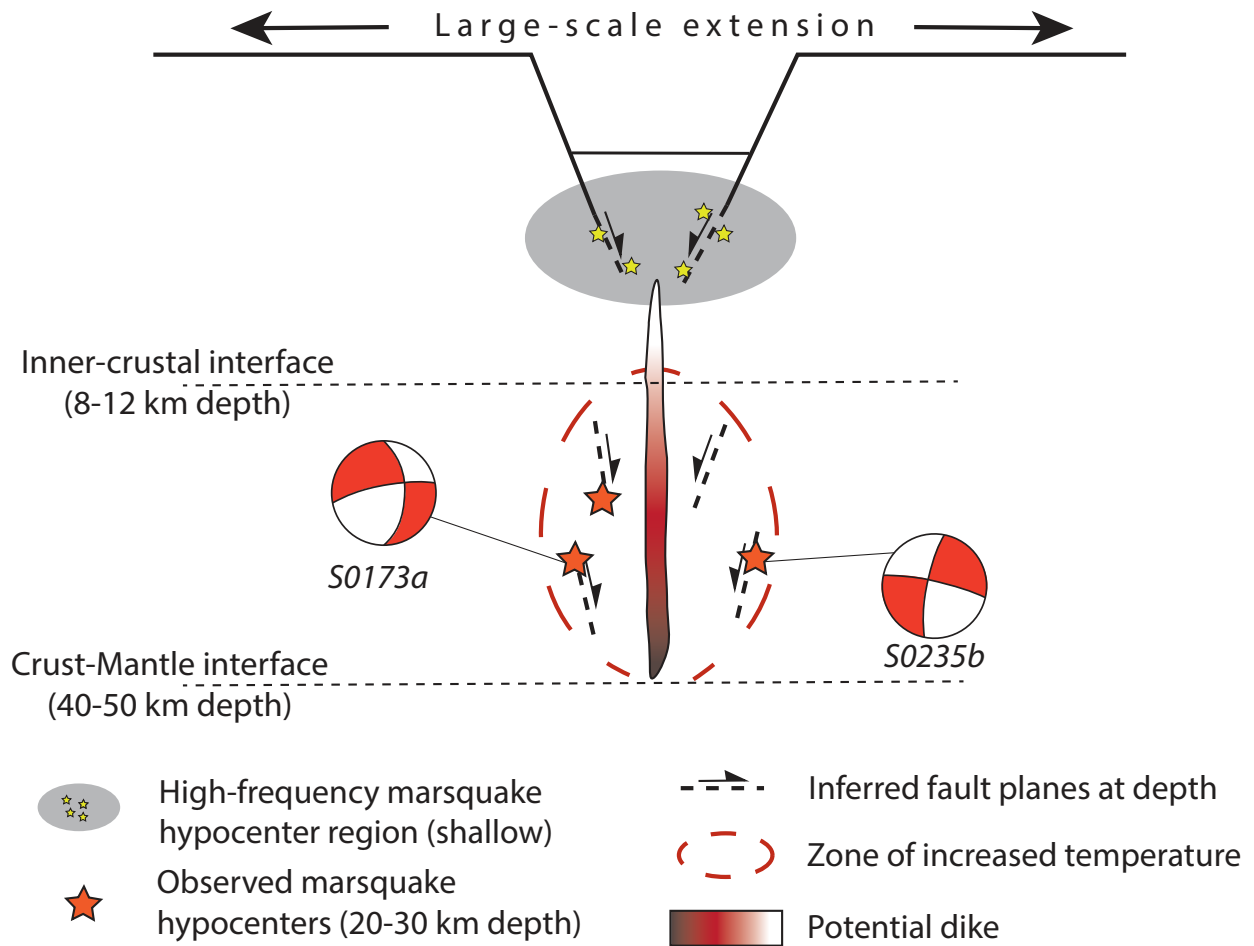


Figure 5: Sketch of an active part of Cerberus Fossae viewed from East. The low frequency marsquake depths indicate faulting in the lower part of the crust, the low stress drop suggests that hypocenters (red stars) are located in the zone of increased temperature (red dashed) around a (recently) active dike at depth. Event S0235b has been previously located to the North of the fault, S0173a to the South. In combination with the focal mechanisms inferred in [12], rupture planes dipping towards the dike are plausible. In the shallow part, high frequency marsquakes are caused by residual stress on the flanks of the graben (yellow stars). The focal mechanisms are plot as seen from 70°azimuth.

Event	Quality	Distance [deg]	M_W	f_c	Back Azimuth [deg]			
					MQS	Uncertainty	Pol.-based	Uncertainty
Events in Cerberus Fossae								
S0173a	A	30.0	3.7 ± 0.3	0.45 ± 0.15	91	79-102	88	78-103
S0235b	A	28.7	3.7 ± 0.2	0.45 ± 0.15	74	66-88	77	64-100
S0802a	B	30.0	2.9 ± 0.2	0.75 ± 0.25	-	-	82	65-96
S0809a	A	29.8	3.3 ± 0.2	0.7 ± 0.3	87	67-105	91	82-100
S0820a	A	30.2	3.3 ± 0.2	0.55 ± 0.25	88	76-107	106	85-120
S0864a	A	28.7	3.1 ± 0.2	0.6 ± 0.2	97	83-116	90	66-110
S0916d	B	29.3	2.9 ± 0.2	0.95 ± 0.35	-	-	97	41-114
S1133c.	A	30.2	3.8 ± 0.2	0.8 ± 0.2	-	-	90	70-110
Events likely in Cerberus Fossae								
<i>S0105a</i>	C	32.5	3.0 ± 0.4	0.5 ± 0.2	-	-	112	95-133
<i>S0325a</i>	B	39.7	3.7 ± 0.3	0.5 ± 0.2	-	-	57	43-73
<i>S0407a</i>	B	29.3	2.9 ± 0.3	0.7 ± 0.2	-	-	57	43-169
<i>S0409d</i>	B	31.1	3.2 ± 0.3	0.5 ± 0.2	-	-	70	50-90
<i>S0474a</i>	C	29.1	2.9 ± 0.3	0.6 ± 0.2	-	-	97	72-123
<i>S0484b</i>	B	31.8	2.9 ± 0.2	0.6 ± 0.3	-	-	100	80-120
<i>S0784a</i>	B	34.5	3.3 ± 0.2	0.8 ± 0.3	-	-	115	92-136
Other marsquakes								
S1102a	A	74	3.6 ± 0.2	2.85 ± 1.0	286	261-309	22	354-55
S0185a	B	59.8	3.1 ± 0.3	1.8 ± 0.6	-	-	-	-

Table 1: Table summarising marsquake parameters. The marsquake events, type (BB = broad-band, LF = low-frequency), distance, M_W , quality (highest to lowest for A, B, C) and MQS back-azimuths are taken from the MQS catalog [14]. MQS uncertainties are described in [13]. Magnitude M_W based on [30]. Polarization back-azimuth values and uncertainties are described in [28]. Events in *italics* have less certain back-azimuth estimates (see [28]).

233 2 Methods

234 Distance

235 Marsquakes are located by the Marsquake Service (MQS; [64]). Their respective distances from the InSight lander are
 236 determined from seismic data in combination with geophysically constrained velocity models, i.e. without taking prior
 237 tectonic information into account. For LF events, MQS uses the arrival time difference between P- and S-waves, the two
 238 strongest seismic body waves to compute the distance of the event from InSight. This travel time difference is compared
 239 to predicted travel times for a suite of inferred one-dimensional velocity-density structure models of Mars' interior
 240 [13, 16, 56]. The uncertainty in absolute distance is a combination of uncertainty in picking the arrival times and the
 241 span of possible seismic velocities in the interior model suite [65]. The uncertainty in seismic velocities from most
 242 recent interior models is about 5% [56]. If one separates the effect of pick uncertainty and velocity model uncertainty,
 243 the relative distances of all marsquakes can be determined with much higher precision than their absolute distances,
 244 allowing to identify a cluster of seismic activity. The absolute distance of this cluster can then be estimated using
 245 different types of interior velocity models (Figure 2a).

246 We use P and S-wave pick times of the MQS catalog version 9 [14] for marsquakes in distances within 3000 km ($\approx 50^\circ$)
 247 of InSight and investigate the distance spread resulting from 2 end member velocity models and one median model
 248 from [29]. The model with slowest/fastest velocities creates the set of *nearby/far* solutions. From these event distances,
 249 we determine a normalized seismicity density over distance (Figure 2a; see A.1). The uncertainty in depth of the events
 250 is estimated to be on the order of 20 km, and is reflected in the distance distributions.

251 For HF events, we use MQS S/P picks (termed Sg and Pg, due to crustal propagation [13]) and according to MQS
 252 practice we assume that the onsets of the two observed phases propagate with velocities of $v_{Pg}=4$ km/s and $v_{Pg}/v_{Sg} = \sqrt{3}$
 253 [13], consistent with velocities of the lower crust [33]. The 286 HF events are spread over a distance range from
 254 1200-2500 km (20 to 40°), with a clear maximum between 1700 and 2000 km (27 and 32° ; see Figure 2a), consistent
 255 with the center of Cerberus Fossae (Figure 2a).

256 Direction

257 Because InSight comprises a single-station global network, the direction towards an LF event (termed back-azimuth)
 258 is estimated independently from the distance. MQS originally uses the linearity of P-wave motion [65], which only
 259 resulted in direction estimates for 8 events, due to the low SNR. A recently proposed more robust alternative is based on
 260 the eigenvalues of the spectral matrix [66] for P- and S-waves [28]. With this approach, we found that at least 14 events
 261 are located within 150 km north/south of Cerberus Fossae as seen from InSight (see table 1). By application of the
 262 method to well-located terrestrial data of similar signal-to-noise ratio, [28] found that this is within the uncertainty of
 263 the method at a distance of 1500 km. Therefore, all these 14 LF marsquakes are compatible with locations in Cerberus
 264 Fossae (Table 1).

265 The direction of HF events has so far been unknown, because the highly scattered first arrival has not shown an increased
 266 degree of polarization for any single event [13, 28]. Here, we make use of the large number of HF events observed so far.
 267 To investigate whether the epicenters of the HF events are in a similar location, we stack all HF event waveforms and
 268 compare horizontal seismogram power in the radial direction of central Cerberus Fossae (70° from North, radial) with
 269 that in the orthogonal direction (transverse). If the sources are indeed located in this direction, we expect the P-wave
 270 arrival to show higher energy in radial direction, at least in a short time window, in which ballistic waves dominate.
 271 Figure 3a shows no clear effect, likely due to time shifts between the phase arrivals of individual events. We follow
 272 [67] and conduct a realignment of the Pg arrivals using a multichannel cross-correlation method [68]. After alignment,
 273 we select 32 events in a distance between 23° and 25° to minimize the variation in backazimuth within the event stack.
 274 We find that the ratio of radial to transverse energy is maximized for a back-azimuth of $78^\circ \pm 12^\circ$, supporting the
 275 identification of Cerberus Fossae as source region of the HF events (see A.2).

276 Spectral character

277 Estimating the source spectrum of a quake is difficult from a single seismic record, because the high-frequency fall-off is
 278 affected by attenuation, both from intrinsic viscoelasticity, Q_i [69, 70], as well as scattering, Q_{scat} [71]. For frequencies
 279 above 1 Hz, scattering has been found to affect P- and S-waves considerably, on Earth [72] and on the Moon [73].
 280 Below 1 Hz, both attenuation mechanisms affect S-waves significantly stronger than P-waves due to longer propagation
 281 time of S-waves. From a single seismic record, one can isolate source effects by correcting the observed spectra for
 282 different values of intrinsic shear wave attenuation $Q_i = Q_\mu$ until the P- and S-spectra match. Doing that, we find that
 283 the P- and S-wave spectra of LF events cannot be explained by effects of intrinsic attenuation alone, but show a strong

284 source imprint. As an example, Figure 4a shows the P-wave spectrum of the high-SNR event S0173a corrected for an
 285 average $Q_\mu = 1000$, requiring a corner frequency $f_c = 0.45 \pm 0.15$ Hz.

286 Following [35, 74], we assume that the source spectrum of a marsquake can be described by

$$A_{\text{src}}(f) = \frac{\Omega_0}{[1 + (f/f_c)^{\gamma n}]^{1/\gamma}}, \quad (2)$$

287 where Ω_0 is the amplitude at long-period, describing the total deformation caused by the event. In the classical definition
 288 of Brune, [35], $\gamma = 1, n = 2$. This fits the theoretical prediction of the Haskell source model of a single patch rupturing
 289 from one side to the other, while elongated faults lead to values of $n > 2$. The corner frequency f_c is related to the
 290 *stress drop* $\Delta\sigma$ by

$$f_c = k\beta \sqrt[3]{\frac{16 \Delta\sigma}{7 M_0}}, \quad (3)$$

291 where β is the shear wave speed, M_0 the scalar moment of the source and k a dimensionless scaling parameter. For
 292 circular ruptures, [75] showed that $k = 0.38, 0.26$ for P- and S-waves, respectively. All else being equal, we therefore
 293 expect the P- and S-wave spectrum to be similar, with a corner frequency that is potentially higher for the P-wave.

294 The measured displacement spectrum at the receiver $A(f)$ is further shaped by viscoelastic attenuation along the path,
 295 described by the intrinsic quality factor $Q(f)$

$$A(f) = A_{\text{src}}(f) \cdot \exp\left(-\pi \frac{fT}{Q(f)}\right) \stackrel{Q(f)=Q_0}{=} A_{\text{src}}(f) \cdot \exp(-\pi ft^*), \quad (4)$$

296 where T is the propagation time. Q generally depends on frequency, often expressed as $Q(f) = Q_0 f^\alpha$ with $\alpha \approx 0.2$
 297 [76]. Over narrow frequency ranges, this effect however can be neglected and we assume a constant $Q(f) = Q_0$. For
 298 the bulk of the Earth, the shear wave attenuation Q_μ^{-1} is significantly higher than the bulk attenuation Q_κ^{-1} , so a typical
 299 assumption is $Q_\kappa = \infty$. For a Poisson solid ($\alpha/\beta = \sqrt{3}$), this means $Q_P = 9/4 Q_\mu = 9/4 Q_S$. If the P- and the S-wave
 300 travel the same path, the ratio of their travel times is $\sqrt{3}$, resulting in $t_P^* \approx t_S^*/4$.

301 A full attenuation model of the Martian mantle and lithosphere including scattering does not exist yet, but we can
 302 assume that all LF marsquakes located in Cerberus Fossae are affected by the same attenuation structure. We therefore
 303 attempt to remove the effect of attenuation (eq. 4) by choosing a value for Q_μ that minimizes the difference between
 304 the P- and the S- spectrum for all LF marsquakes located in Cerberus Fossae. Following [17], we assume that the
 305 propagation path for HF events is shallow and different compared to the LF events and therefore, a different average
 306 Q_μ applies. After selecting these values for attenuation, we expect to be left with a reasonable estimate of the pure
 307 source spectrum, from which we can infer the corner frequency, f_c . Given the low signal-to-noise ratio and limited
 308 bandwidth of the Martian data (see fig. 4), we assume for simplicity that the corner frequencies for P- and S-waves are
 309 identical. Further, we fix $\gamma = 1$ and only try to match for f_c and n .

310 To summarize: We correct for attenuation using

$$A_S(f) = \underbrace{A_{0,S}}_{A_{\text{src},S}(f)} \underbrace{\frac{1}{1 + (f/f_c)^n} \exp\left(-\frac{\pi f T_S}{Q_S}\right)}_{A_{\text{att},S}(f)} \quad (5)$$

311 and

$$A_P(f) = \xi A_{\text{src},S}(f) A_{\text{att},S}^{-(1/4)}(f), \quad (6)$$

312 where ξ is the zero-frequency P/S ratio, which depends mainly on the focal mechanism, as well as on the wave velocities
 313 at the source. Since it is a constant offset, we fix it such, that the long-period part of P- and S-spectra match here.

314 We compute the spectra of P- and S-waves from a 30 second time window starting 10 seconds before the respective
 315 MQS pick. The short time window is chosen to mitigate the effect of lithospheric scattering. An additional noise
 316 spectrum is computed from a 60 second time window before the event to select a suitable frequency window for each
 317 individual event. The matching between observed $A_{\text{src},P}(f)$ and eq. 2 is done manually for each event. We find that a
 318 value of $Q_\mu = 1000$, equivalent to $Q_P = 2250$ produces a reasonable match between P- and S-wave spectra. This is
 319 not to be understood as a final value for the intrinsic attenuation of the mantle, but just as a value where source effects
 320 can be studied reasonably well. Figures 6 and 7 show that the value of $Q \approx 400$ proposed by [11] cannot explain both
 321 P- and S-spectra well and must be seen as an "effective Q", describing the spectral decay and thereby combining effects
 322 of source and structure (as written therein). The supplementary section A.5 contains figures of observed spectra and
 323 matching source functions for the events discussed in this manuscript. We manually match two corner frequencies f_c to
 324 each event, a reasonable maximum and minimum, with a fixed slope of $n = 2.5$. For the final dataset in table 1 and
 325 figure 4, we add an additional 0.1 to the uncertainty to account for the limited SNR of all events.

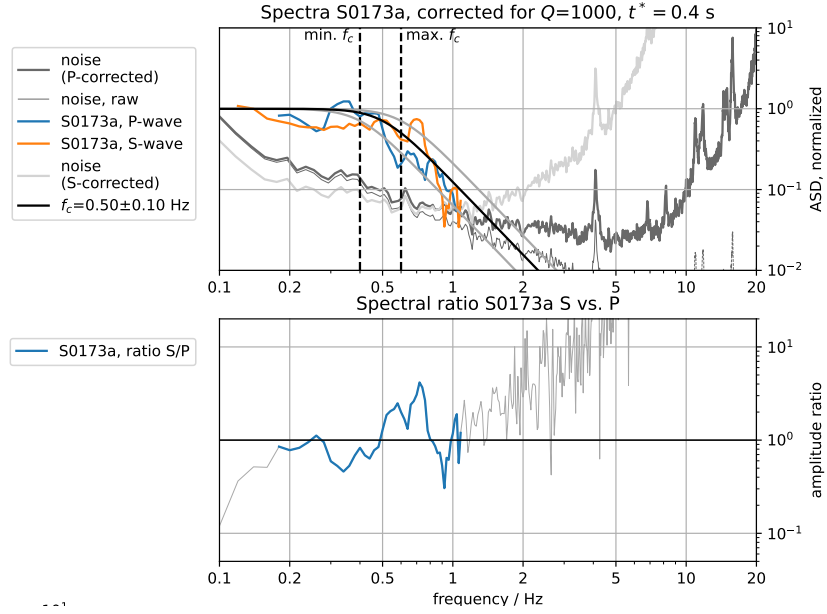


Figure 6: Event S0173a, after correction for Q_μ (eq. 5, 6). Top: The value of $Q_\mu = 1000$ has been chosen to make P and S-wave spectra match. Each spectrum was computed in a time window of 30 second length around the arrival using a multitaper method [77]. The S-wave and P-wave amplitude spectra meet the pre-event noise at 1.1 Hz. For easier comparison, the noise spectra are plotted 3 times: (i) raw, and using the correction terms for (ii) P- and (iii) S-waves. Bottom: Ratio of P- and S-wave spectrum. The colored part highlights the frequency range in which both P- and S-wave are above noise. The black line marks a theoretical spectrum (eq. 2) with $f_c = 0.5$ Hz and $n = 2$.

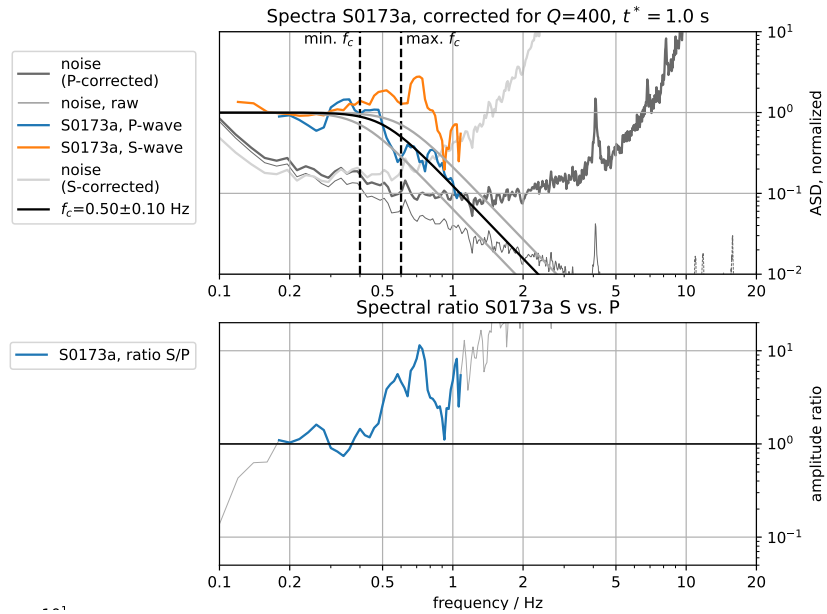


Figure 7: Event S0173a, with the attenuation model of [11]. The value of $Q_\mu = 400$ leads to a significant over-prediction of the S-wave amplitude above 0.5 Hz.

References:

- 326
- 327 1. Knapmeyer, M. *et al.* Working Models for Spatial Distribution and Level of Mars' Seismicity. *Journal of*
328 *Geophysical Research E: Planets* **111**, 1–23 (2006).
 - 329 2. Tanaka, K. L. *et al.* Geologic Map of Mars. *U.S. Geological Survey Geologic Investigations*, 3292–3292 (2014).
 - 330 3. Lognonné, P. *et al.* SEIS: Insight's Seismic Experiment for Internal Structure of Mars. *Space Science Reviews*
331 **215**, 12–12 (Jan. 2019).
 - 332 4. Banerdt, W. B. *et al.* Initial Results from the InSight Mission on Mars. *Nature Geoscience* **13**, 183–189 (Mar.
333 2020).
 - 334 5. Golombek, M. P. *et al.* Geology of the InSight Landing Site on Mars. *Nature Communications* **11**, 1–11 (2020).
 - 335 6. Phillips, R. J. *Expected Rate of Marsquakes* tech. rep. (1991), 35–38.
 - 336 7. Gudkova, T. V., Batov, A. V. & Zharkov, V. N. Model Estimates of Non-Hydrostatic Stresses in the Martian Crust
337 and Mantle: 1—Two-Level Model. *Solar System Research* **51**, 457–478 (Nov. 2017).
 - 338 8. Berman, D. C. & Hartmann, W. K. Recent Fluvial, Volcanic, and Tectonic Activity on the Cerberus Plains of
339 Mars. *Icarus* **159**, 1–17 (Sept. 2002).
 - 340 9. Anderson, R. C. *et al.* Primary Centers and Secondary Concentrations of Tectonic Activity through Time in the
341 Western Hemisphere of Mars. *Journal of Geophysical Research: Planets* **106**, 20563–20585 (2001).
 - 342 10. Lognonné, P. *et al.* Constraints on the Shallow Elastic and Anelastic Structure of Mars from InSight Seismic Data.
343 *Nature Geoscience* **13**, 213–220 (Mar. 2020).
 - 344 11. Giardini, D. *et al.* The Seismicity of Mars. *Nat. Geosci.* **13**, 205–212 (Mar. 2020).
 - 345 12. Brinkman, N. *et al.* First Focal Mechanisms of Marsquakes. *Journal of Geophysical Research: Planets* (2021).
 - 346 13. Clinton, J. F. *et al.* The Marsquake Catalogue from InSight, Sols 0–478. *Physics of the Earth and Planetary*
347 *Interiors* **310** (2021).
 - 348 14. Service, I. M. *Mars Seismic Catalogue, InSight Mission; V6 2021-04-01 2021.*
 - 349 15. Jacob, A. *et al.* Seismic Sources of InSight Marsquakes and Seismotectonic Context of Elysium Planitia, Mars.
350 *Tectonophysics*, 229434 (June 2022).
 - 351 16. Stähler, S. C. *et al.* Seismic Detection of the Martian Core. *Science* **373**, 443–448 (July 2021).
 - 352 17. van Driel, M. *et al.* High-Frequency Seismic Events on Mars Observed by InSight. *Journal of Geophysical*
353 *Research: Planets* **126**, e2020JE006670 (2021).
 - 354 18. Horleston, A. *et al.* The Far Side of Mars - Two Distant Marsquakes Detected by InSight. *The seismic record* **2**,
355 88–99 (2022).
 - 356 19. Perrin, C. *et al.* Geometry and Segmentation of Cerberus Fossae, Mars: Implications for Marsquake Properties.
357 *Journal of Geophysical Research: Planets* **127**, e2021JE007118 (2022).
 - 358 20. Head, J. W. Generation of Recent Massive Water Floods at Cerberus Fossae, Mars by Dike Emplacement,
359 Cryospheric Cracking, and Confined Aquifer Groundwater Release. *Geophys. Res. Lett.* **30**, 1577 (2003).
 - 360 21. Burr, D. M. Recent Aqueous Floods from the Cerberus Fossae, Mars. *Geophys. Res. Lett.* **29**, 1013 (2002).
 - 361 22. Taylor, J., Teanby, N. A. & Wookey, J. Estimates of Seismic Activity in the Cerberus Fossae Region of Mars.
362 *Journal of Geophysical Research E: Planets* **118**, 2570–2581 (2013).
 - 363 23. Voigt, J. R. C. & Hamilton, C. W. Investigating the Volcanic versus Aqueous Origin of the Surficial Deposits in
364 Eastern Elysium Planitia, Mars. *Icarus* **309**, 389–410 (July 2018).
 - 365 24. Horvath, D. G., Moitra, P., Hamilton, C. W., Craddock, R. A. & Andrews-Hanna, J. C. Evidence for Geologically
366 Recent Explosive Volcanism in Elysium Planitia, Mars. *Icarus* **365**, 114499 (Sept. 2021).
 - 367 25. Banerdt, W. B., Golombek, M. P. & Tanaka, K. L. Stress and Tectonics on Mars. *In: Mars (A93-27852 09-91)*, p.
368 249-297., 249–297 (1992).
 - 369 26. Hauber, E., Brož, P., Jagert, F., Jodłowski, P. & Platz, T. Very Recent and Wide-Spread Basaltic Volcanism on
370 Mars. *Geophysical Research Letters* **38**, n/a–n/a (2011).
 - 371 27. Plesa, A.-C., Wiczczonek, M., Knapmeyer, M., Walterova, M. & Breuer, D. in *Geophysical Exploration of the*
372 *Solar System* (Elsevier, May 2022).
 - 373 28. Zenhäusern, G. *et al.* Low-Frequency Marsquakes and Where to Find Them: Back Azimuth Determination Using
374 a Polarization Analysis Approach. *Bulletin of the Seismological Society of America* (May 2022).
 - 375 29. Stähler, S. C., Khan, A., Drilleau, M., Duran, A. C. & Samuel, H. *Interior Models of Mars from Inversion of*
376 *Seismic Body Waves* 2021.
 - 377 30. Böse, M. *et al.* Magnitude Scales for Marsquakes Calibrated from InSight Data. *Bulletin of the Seismological*
378 *Society of America* (June 2021).

- 379 31. Knapmeyer, M. *et al.* Seasonal Seismic Activity on Mars. *Earth and Planetary Science Letters* **576**, 117171 (Dec.
380 2021).
- 381 32. Knapmeyer, M. *et al.* Estimation of the Seismic Moment Rate from an Incomplete Seismicity Catalog, in the
382 Context of the InSight Mission to Mars. *Bulletin of the Seismological Society of America* **109**, 1125–1147 (2019).
- 383 33. Knapmeyer-Endrun, B. *et al.* Thickness and Structure of the Martian Crust from InSight Seismic Data. *Science*
384 **373**, 438–443 (July 2021).
- 385 34. Vetterlein, J. & Roberts, G. P. Structural Evolution of the Northern Cerberus Fossae Graben System, Elysium
386 Planitia, Mars. *Journal of Structural Geology* **32**, 394–406 (Apr. 2010).
- 387 35. Brune, J. N. Tectonic Stress and the Spectra of Seismic Shear Waves from Earthquakes. *Journal of Geophysical*
388 *Research (1896-1977)* **75**, 4997–5009 (1970).
- 389 36. Abercrombie, R. E. Earthquake Source Scaling Relationships from -1 to 5 ML Using Seismograms Recorded at
390 2.5-Km Depth. *Journal of Geophysical Research: Solid Earth* **100**, 24015–24036 (1995).
- 391 37. Allmann, B. P. & Shearer, P. M. Global Variations of Stress Drop for Moderate to Large Earthquakes. *Journal of*
392 *Geophysical Research: Solid Earth* **114** (2009).
- 393 38. Compaire, N. *et al.* Autocorrelation of the Ground Vibrations Recorded by the SEIS-InSight Seismometer on
394 Mars. *Journal of Geophysical Research: Planets* **126**, e2020JE006498 (2021).
- 395 39. Laske, G., Masters, G., Ma, Z. & Pasyanos, M. *Update on CRUST1.0 - A 1-Degree Global Model of Earth's Crust*
396 *in Geophysical Research Abstracts* (2013), EGU2013–2658.
- 397 40. Durán, C. *et al.* Seismology on Mars: An Analysis of Direct, Reflected, and Converted Seismic Body Waves with
398 Implications for Interior Structure. *Physics of the Earth and Planetary Interiors* **325**, 106851 (Apr. 2022).
- 399 41. Drilleau, M. *et al.* Marsquake Locations and 1-D Seismic Models for Mars from InSight Data. *Journal of*
400 *Geophysical Research (Planets)* **accepted** (2022).
- 401 42. Abercrombie, R. E. Resolution and Uncertainties in Estimates of Earthquake Stress Drop and Energy Release.
402 *Philosophical Transactions of the Royal Society A: Mathematical, Physical and Engineering Sciences* **379**,
403 20200131 (May 2021).
- 404 43. Giampiccolo, E., D'Amico, S., Patane, D. & Gresta, S. Attenuation and Source Parameters of Shallow Mi-
405 croearthquakes at Mt. Etna Volcano, Italy. *Bulletin of the Seismological Society of America* **97**, 184–197 (Feb.
406 2007).
- 407 44. Vallée, M. Source Time Function Properties Indicate a Strain Drop Independent of Earthquake Depth and
408 Magnitude. *Nature Communications* **4**, 2606–2606 (2013).
- 409 45. Oberst, J. Unusually High Stress Drops Associated with Shallow Moonquakes. *Journal of Geophysical Research*
410 **92**, 1397–1405 (1987).
- 411 46. Hensch, M. *et al.* Deep Low-Frequency Earthquakes Reveal Ongoing Magmatic Recharge beneath Laacher See
412 Volcano (Eifel, Germany). *Geophysical Journal International* **216**, 2025–2036 (Mar. 2019).
- 413 47. Chouet, B. A. & Matoza, R. S. A Multi-Decadal View of Seismic Methods for Detecting Precursors of Magma
414 Movement and Eruption. *Journal of Volcanology and Geothermal Research* **252**, 108–175 (Feb. 2013).
- 415 48. Kedar, S. *et al.* Analyzing Low Frequency Seismic Events at Cerberus Fossae as Long Period Volcanic Quakes.
416 *Journal of Geophysical Research: Planets* **126**, e2020JE006518 (2021).
- 417 49. Madariaga, R. Dynamics of an Expanding Circular Fault. *Bulletin of the Seismological Society of America* **66**,
418 639–666 (1976).
- 419 50. Roberts, G. P., Matthews, B., Bristow, C., Guerrieri, L. & Vetterlein, J. Possible Evidence of Paleomarsquakes
420 from Fallen Boulder Populations, Cerberus Fossae, Mars. *Journal of Geophysical Research: Planets* **117**, n/a–n/a
421 (Feb. 2012).
- 422 51. Kolzenburg, S. *et al.* Solid as a Rock: Tectonic Control of Graben Extension and Dike Propagation. *Geology* **50**,
423 260–265 (Nov. 2021).
- 424 52. Watters, T. R. *et al.* Shallow Seismic Activity and Young Thrust Faults on the Moon. *Nature Geoscience* **12**,
425 411–417 (2019).
- 426 53. Plesa, A.-C. *et al.* Present-Day Mars' Seismicity Predicted From 3-D Thermal Evolution Models of Interior
427 Dynamics. *Geophysical Research Letters* **45**, 2580–2589 (Mar. 2018).
- 428 54. Bergman, E. A. Intraplate Earthquakes and the State of Stress in Oceanic Lithosphere. *Tectonophysics* **132**, 1–35
429 (Dec. 1986).
- 430 55. Clauser, C. & Huenges, E. in *Rock Physics & Phase Relations* 105–126 (American Geophysical Union (AGU),
431 1995). ISBN: 978-1-118-66810-8.
- 432 56. Khan, A. *et al.* Imaging the Upper Mantle Structure of Mars with InSight Seismic Data. *Science* **373**, 434–438
433 (2021).

- 434 57. Byrne, P. K. A Comparison of Inner Solar System Volcanism. *Nature Astronomy* **4**, 321–327 (2020).
- 435 58. Smith, D. E. *et al.* Mars Orbiter Laser Altimeter: Experiment Summary after the First Year of Global Mapping of
436 Mars. *Journal of Geophysical Research: Planets* **106**, 23689–23722 (2001).
- 437 59. Dahmen, N. L. *et al.* Resonances and Lander Modes Observed by InSight on Mars (1–9 Hz). *Bulletin of the*
438 *Seismological Society of America* **111**, 2924–2950 (Oct. 2021).
- 439 60. Hobiger, M. *et al.* The Shallow Structure of Mars at the InSight Landing Site from Inversion of Ambient Vibrations.
440 *Nat Commun* **12**, 6756 (Nov. 2021).
- 441 61. Iio, Y. SCALING RELATION BETWEEN EARTHQUAKE SIZE AND DURATION OF FAULTING FOR
442 SHALLOW EARTHQUAKES IN SEISMIC MOMENT BETWEEN 10^{10} AND 10^{25} Dyne•cm. *Journal of*
443 *Physics of the Earth* **34**, 127–169 (1986).
- 444 62. Bilek, S. L., Lay, T. & Ruff, L. J. Radiated Seismic Energy and Earthquake Source Duration Variations from
445 Teleseismic Source Time Functions for Shallow Subduction Zone Thrust Earthquakes. *Journal of Geophysical*
446 *Research: Solid Earth* **109** (2004).
- 447 63. Matsuzawa, T., Obara, K. & Maeda, T. Source Duration of Deep Very Low Frequency Earthquakes in Western
448 Shikoku, Japan. *Journal of Geophysical Research: Solid Earth* **114** (2009).
- 449 64. Clinton, J. F. *et al.* The Marsquake Service: Securing Daily Analysis of SEIS Data and Building the Martian
450 Seismicity Catalogue for InSight. *Space Science Reviews* **214**, 133–133 (Dec. 2018).
- 451 65. Böse, M. *et al.* A Probabilistic Framework for Single-Station Location of Seismicity on Earth and Mars. *Physics*
452 *of the Earth and Planetary Interiors* **262**, 48–65 (2016).
- 453 66. Schimmel, M. & Gallart, J. The Use of Instantaneous Polarization Attributes for Seismic Signal Detection and
454 Image Enhancement. *Geophysical Journal International* **155**, 653–668 (2003).
- 455 67. Kim, D. *et al.* Improving Constraints on Planetary Interiors With PPs Receiver Functions. *Journal of Geophysical*
456 *Research: Planets* **126**, e2021JE006983 (2021).
- 457 68. VanDecar, J. C. & Crosson, R. S. Determination of Teleseismic Relative Phase Arrival Times Using Multi-Channel
458 Cross-Correlation and Least Squares. *Bulletin of the Seismological Society of America* **80**, 150–169 (Feb. 1990).
- 459 69. Kane, D. L., Prieto, G., Vernon, F. L. & Shearer, P. M. Quantifying Seismic Source Parameter Uncertainties.
460 *Bulletin of the Seismological Society of America* **101**, 535–543 (Mar. 2011).
- 461 70. Trugman, D. T., Dougherty, S. L., Cochran, E. S. & Shearer, P. M. Source Spectral Properties of Small to Moderate
462 Earthquakes in Southern Kansas. *Journal of Geophysical Research: Solid Earth* **122**, 8021–8034 (2017).
- 463 71. Aki, K. & Chouet, B. Origin of Coda Waves: Source, Attenuation, and Scattering Effects. *Journal of Geophysical*
464 *Research* **80**, 3322–3342 (1975).
- 465 72. Yoshimoto, K., Sato, H. & Ohtake, M. Frequency-Dependent Attenuation of P and S Waves in the Kanto Area,
466 Japan, Based on the Coda-Normalization Method. *Geophysical Journal International* **114**, 165–174 (July 1993).
- 467 73. Nakamura, Y. & Koyama, J. Seismic Q of the Lunar Upper Mantle. *Journal of Geophysical Research* **87**, 4855–
468 4861 (1982).
- 469 74. Boatwright, J. Seismic Estimates of Stress Release. *Journal of Geophysical Research: Solid Earth* **89**, 6961–6968
470 (Aug. 1984).
- 471 75. Kaneko, Y. & Shearer, P. M. Seismic Source Spectra and Estimated Stress Drop Derived from Cohesive-Zone
472 Models of Circular Subshear Rupture. *Geophysical Journal International* **197**, 1002–1015 (May 2014).
- 473 76. Baig, A. M., Dahlen, F. A. & Hung, S.-H. Traveltimes of Waves in Three-Dimensional Random Media. *Geophys-*
474 *ical Journal International* **153**, 467–482 (May 2003).
- 475 77. Prieto, G., Parker, R. L. & Vernon, F. L. A Fortran 90 Library for Multitaper Spectrum Analysis. *Computers &*
476 *Geosciences* **35**, 1701–1710 (Aug. 2009).
- 477 78. Ceylan, S. *et al.* Companion Guide to the Marsquake Catalog from InSight, Sols 0–478: Data Content and
478 Non-Seismic Events. *Physics of the Earth and Planetary Interiors* **310**, 106597–106597 (Jan. 2021).
- 479 79. Scholz, J.-R. *et al.* Detection, Analysis, and Removal of Glitches From InSight’s Seismic Data From Mars. *Earth*
480 *and Space Science* **7**, 1–31 (Nov. 2020).
- 481 80. Kim, D. *et al.* Potential Pitfalls in the Analysis and Structural Interpretation of Seismic Data from the Mars InSight
482 Mission. *Bulletin of the Seismological Society of America* **111**, 2982–3002 (Oct. 2021).
- 483 81. Kagan, Y. Y. Seismic Moment Distribution Revisited: I. Statistical Results. *Geophysical Journal International*
484 **148**, 520–541 (Mar. 2002).

485 **A Supplement**

486 **A.1 Distribution of marsquakes**

487 Probability density functions for distance and back azimuth for LF events are taken from models in [29] and [28].
488 Figure 2 only shows distance distributions for all investigated events using different interior models, thus leading
489 to far and near end-member models and a mean model. In Figure 1 we multiply the normalized mean distance and
490 back-azimuth distributions. For HF, we show the distance distribution in Figure 2a. For Figure 1, we use a back azimuth
491 of 78 ± 12 deg (see A.2) and the black box highlights the 80% density line inferred for by distance estimates within the
492 back-azimuth range.

493 A.2 Back azimuth estimates of the HF event cluster

494 All Marsquake Service (MQS) HF events with event quality C or above are used in this analysis [14]. For each event, we
 495 use a standard algorithm of STA/LTA (Short Time Average over Long Time Average) triggering on the corresponding
 496 energy envelope averaged across ZNE components to pick Pg- and Sg-arrivals [hereby referred as the MQS picks, e.g.
 497 11, 13]. Here, our energy envelope is computed for instrument-removed velocity waveforms in the spectral domain
 498 using a 30 s window with 90% overlap. We remove noticeable glitches and donks [see detailed description of these
 499 electro-mechanical signals in e.g. 78–80] within our analysis window between the Pg- and Sg-arrival times. In addition,
 500 we discard those events for which spectral envelopes significantly deviate from the mean envelope of all HF event data.
 501 62 out of 116 events with corresponding correlation coefficients < 0.8 are therefore not considered in the analysis. Next,
 502 the initial alignment guided by the MQS picks is refined for both Pg- and Sg-arrival times systematically using an
 503 implementation of a multichannel cross-correlation method [68] in order to obtain precisely aligned waveform data
 504 with our updated picks (Fig. 8A-B). A pick uncertainty is assigned based on the duration of the amplitude rise time
 505 for each spectral envelope (starting from the onset until the amplitude reaches its maximum). Figure 8C shows the
 506 comparison of the relocated vs. the MQS distance estimates with velocities of $v_{Pg} = 4$ km/s and $v_{Pg}/v_{Sg} = \sqrt{3}$. The
 507 observed difference in the two sets of distance estimates is small, with the mean and standard deviation of the MQS
 508 vs. relocated distances being 24.7 ± 2.9 deg and 24.0 ± 2.6 deg, respectively. To estimate the dominant direction of
 509 seismic energy traveling from the HF event cluster, we perform a grid search on back azimuths that maximize the
 510 median power ratio between the radial vs. transverse component within -30 s to 30 s of the aligned Pg-arrivals across
 511 multiple HF events simultaneously (e.g., data bounded by the red lines in Fig. 8A-B). A similar approach has been
 512 successfully applied to individual LF/BB marsquake data in a recent receiver function analysis [10, 33, 67]. Further,
 513 we apply a 2 s moving-window to compute the power ratio at each time for all 62 HF events and obtain the weighted
 514 median power ratio. In this process, we use relative weights for our HF events based on the signal-to-noise of each
 515 individual event. The average background power ratio is estimated by (i) stacking those values computed within the
 516 pre-event noise window (i.e., values between -30 s and 0 s) and (ii) subtracting those from our resulting power ratios
 517 (Fig. 9). Our back azimuth search on HF data aligned by the MQS picks did not show any prominent arrivals in the -30
 518 to 30 s search window (Fig. 9A). However, we observe that the maximum power ratio is strongly focused at the back
 519 azimuth value of 78 ± 12 deg once our events are systematically re-aligned (c.f., Fig. 9A-B) despite a number of weak
 520 scattered maxima in the time window. Notably, energy arriving after ≈ 20 s becomes much more apparent when we
 521 repeat the analysis using a subgroup of HF events which forms the largest sample size within the event cluster (Fig. 9C).
 522 The time axis in this plot is shifted arbitrarily due to the realignment.

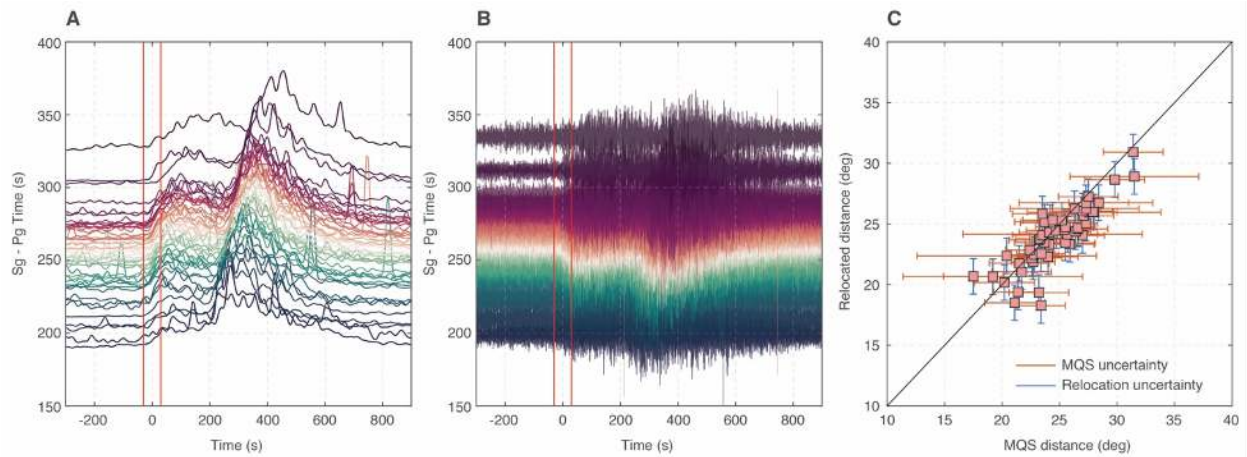


Figure 8: (A) Average three-component envelopes aligned on Pg-arrival ($t = 0$ s) from a total of 62 marsquakes from the HF event category, and the corresponding (B) vertical component waveforms. All MQS events with the event quality C or above are selected between Sols 128 and 1050 [14] but those with low envelope similarity (i.e., correlation coefficient < 0.8 against the mean envelope of all HF event data) are removed. (C) Comparison of the MQS vs. relocated distance estimates with $v_{Pg}=4$ km/s and $v_{Pg}/v_{Sg}=\sqrt{3}$.

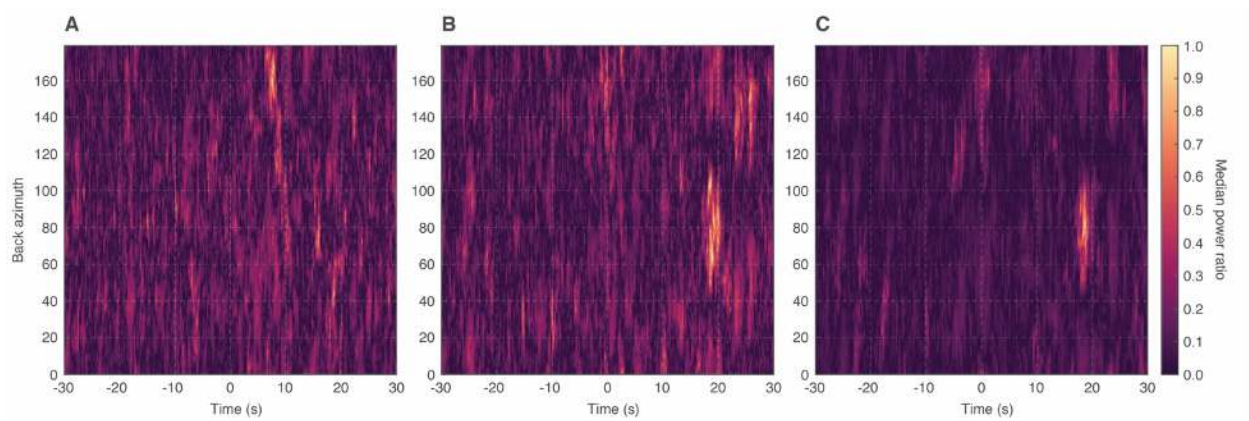


Figure 9: Median power ratio between radial and transverse components of the HF waveforms (A) before, and (B) after applying the re-alignment using average spectral envelopes. (C) Same as (B) but using a subgroup of HF events that clustered tightly at the mean relocated distance of 24° . Background power which is strongly affected by wind noise and lander resonances is removed.

523 A.3 Estimating total moment rate

524 Estimating the long term average moment release rate from an incomplete catalog is affected by the annual variability
 525 of moment release that even a perfectly Poissonian distribution of quakes shows.

526 We first test the distribution for derivation from a Poisson process, by plotting the cumulative count of events over time
 527 and the lag time between events (Fig. 10) and while we find an increased rate in the second year, both years show no
 528 significant deviation from a Poisson process. For the annual rate, we follow the approach presented in [32] to estimate
 529 the parameters of a tapered Gutenberg-Richter size-frequency distribution [81]: The cumulative number of earthquakes
 530 Φ above a magnitude M is then given by

$$\Phi(M) = \left(\frac{M_t}{M}\right) \beta \exp\left(\frac{M_t - M}{M_c}\right) \quad (7)$$

531 In this equation, β is the slope of the power law, describing the distribution of larger to smaller quakes, M_t describes
 532 the magnitude above which the distribution tapers, i.e. larger events occur less often than expected by the power law
 533 and M_c is the magnitude of completeness of the catalog. The total annual moment release M_S can then be estimated
 534 from these parameters, as described in [32].

535 For the events observed in Cerberus Fossae, we assume a slope $\beta = 2/3$, equivalent to a b -value of 1. We use the
 536 KS_{10} estimator from [32] that uses the 10 largest events of a catalog with unknown M_c . We further need to take into
 537 account that only during 26% of the observation time, the local atmospheric conditions were quiet enough to observe
 538 marsquakes. To account for magnitude uncertainty, the analysis was repeated 10,000 times with individual event
 539 magnitudes randomly varied according to their estimated uncertainty [30] in the MQS catalog v9.

540 The resulting estimate of corner magnitude and moment rate are shown in Figure 11, using the KS_{10} estimator of [32],
 541 in the same style as Figures 4, 7 therein. The estimated long term moment rate is $2.93 \cdot 10^{15}$ Nm/a, with an 80% interval
 542 between $1.35 \cdot 10^{15}$ Nm/a and $5.52 \cdot 10^{15}$ Nm/a (Figure 12).

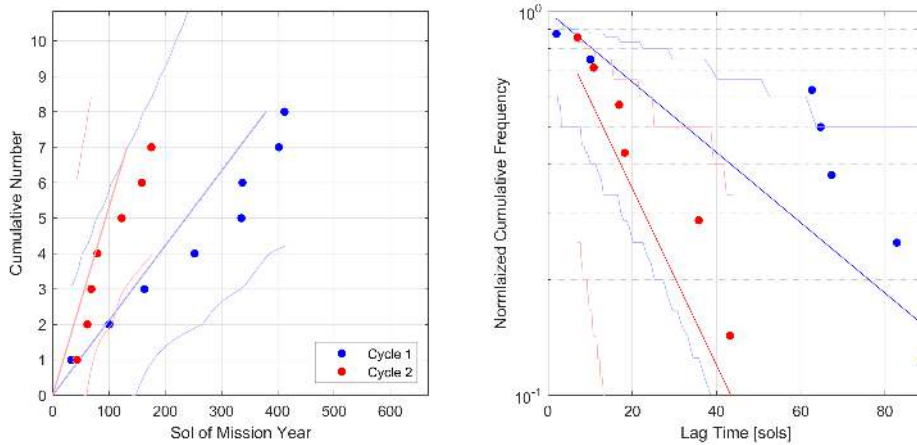


Figure 10: Cumulative count of events (left), and lag time distribution (right). For a stationary Poisson process, the cumulative count as function of time should follow a straight line in linear coordinates. The event rate defines the slope of this line. For the first year of operation (cycle 1, blue), we corrected the count after the three weeks down time in August/September 2019 by assuming that the rate during the down time equalled that afterwards. After Sol 400, increasing wind speeds at night made detection impossible until the second Martian year, starting around Sol 700. For the second year (cycle 2), no such correction was necessary. Pale lines indicate the nominal slope (cycle 1: 0.021 ± 0.007 events/sol, cycle 2: 0.053 ± 0.02 events/sol) and the 95% confidence intervals for likely scatter. The event series end with the end of the catalog (MQS v9). The lag times of a stationary Poisson process are exponentially distributed and thus follow a straight line in a semi-logarithmic plot. Lag times shorter than 1 sol were not considered; the daily noise regime makes them unreliable. All confidence were intervals estimated numerically from $1e5$ synthetic event sequences with the same rate and covering the same duration.

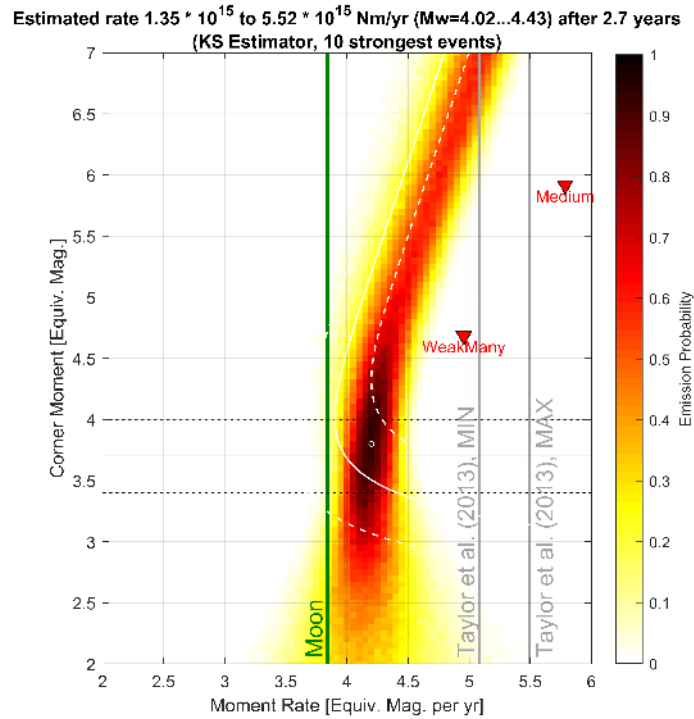


Figure 11: Emission probability of moment rate and corner moment taking into account the 10 largest events observed over the mission until 2021-12-31, using the KS10 estimator of [32], in the same style as figs. 4, 7 therein. For orientation, the moment release of the whole moon, as seen by the Apollo seismic network over 7 years of operation [45] (green) and the moment rates estimated by [22] for Cerberus Fossae (grey) are shown, as well as 2 global estimates from [1] (Many weak faults and the medium model).

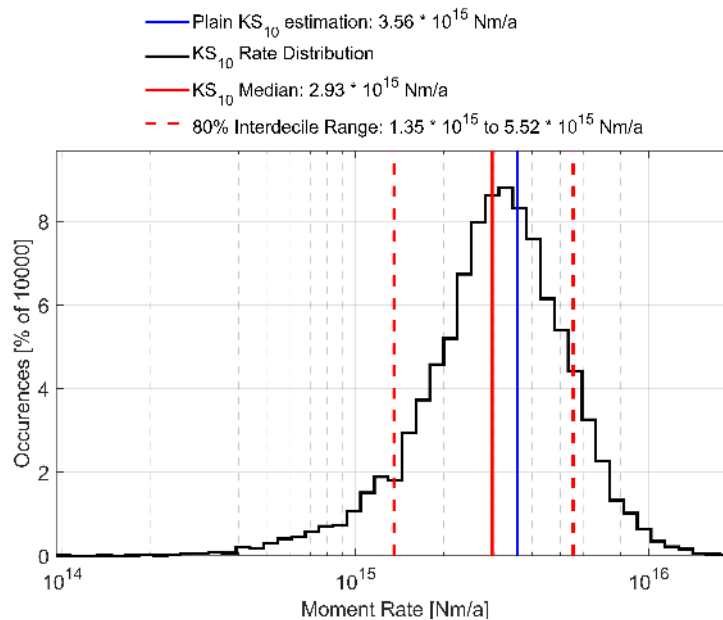


Figure 12: Distribution of annual moment release rate \dot{M} resulting from the emission probability in Figure 11.

543 **A.4 Global fault map**

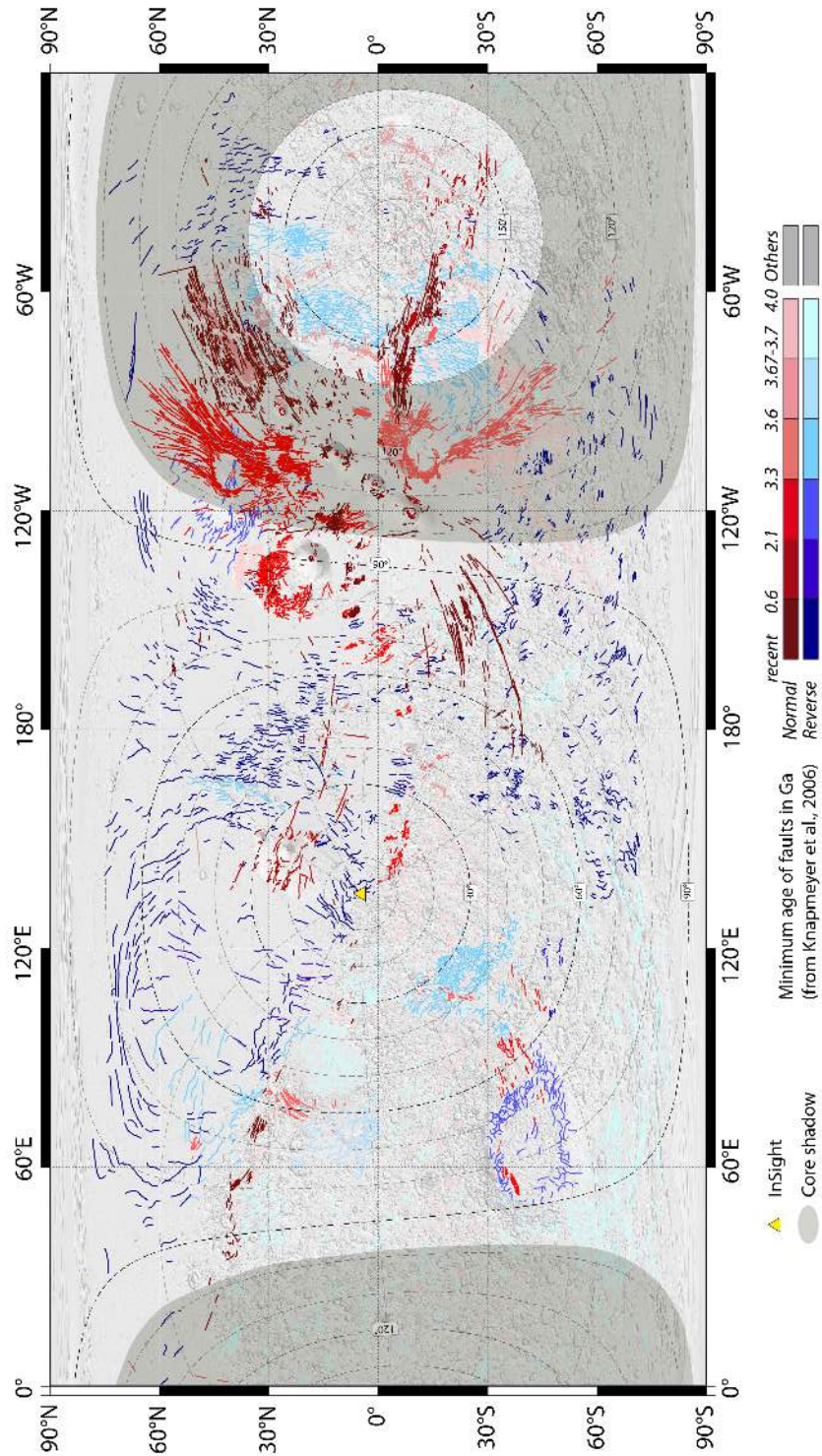


Figure 13: Global map of faults color-coded by minimum age [1, 2, 58]. The darkened area marks the core shadow [16], in which no direct body waves can be observed as seen from InSight. Thus event detection is significantly more difficult.

544 **A.5 Figures of spectral matching**

545 **A.5.1 Events in Cerberus Fossae**

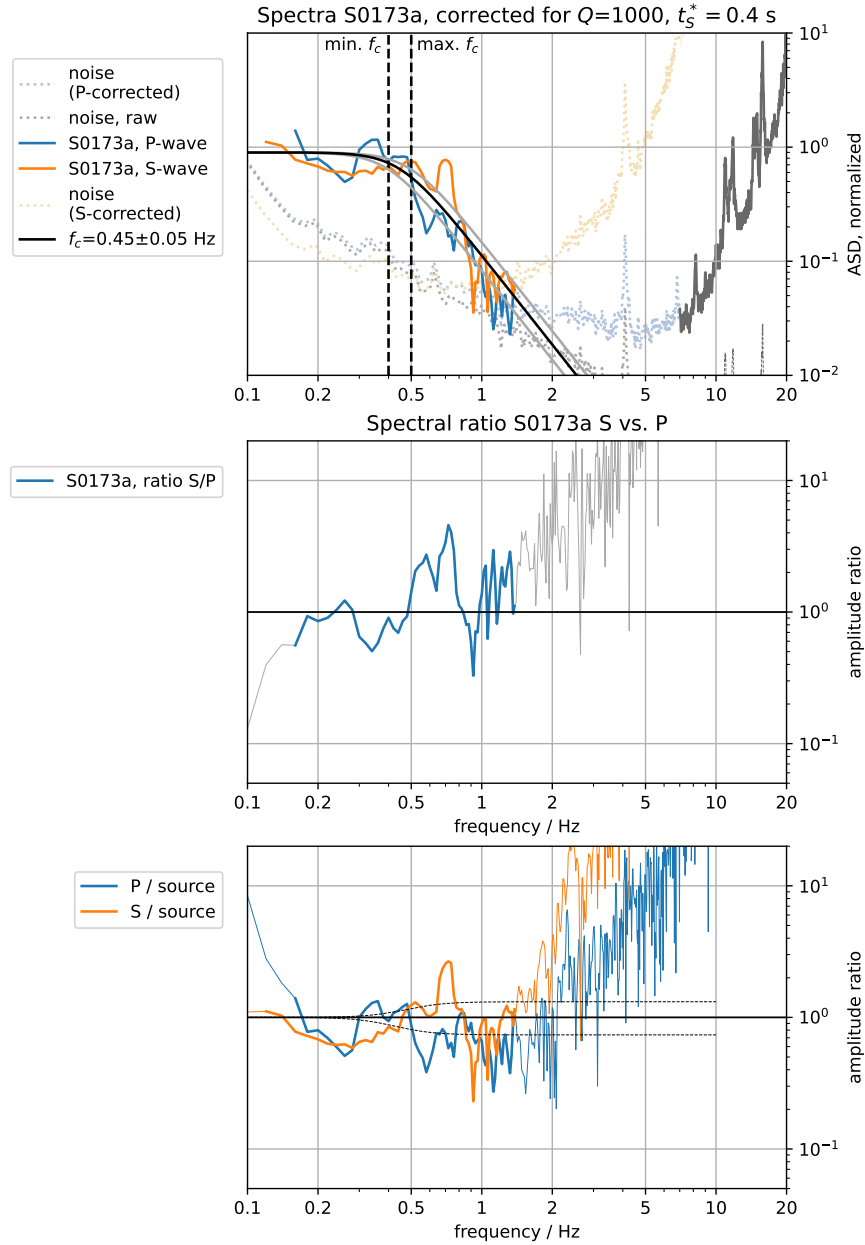


Figure 14: Event S0173a, after correction for Q_μ (eq. 5, 6). Top: The value of $Q_\mu = 1000$ has been chosen to make P and S-wave spectra match after attenuation correction. Each spectrum was computed in a time window of 30 second length around the arrival (-10s to 20s) using a multitaper method [77]. The S-wave and P-wave amplitude spectra meet the pre-event noise at 1.1 Hz. For easier comparison, P and S spectra are normalized individually and the noise spectra are plotted 3 times: (i) raw, and using the correction terms for (ii) P- and (iii) S-waves. The black line marks a theoretical spectrum (eq. 2) with $f_c = 0.45$ Hz and $n = 2.5$. Grey lines mark the range of source spectra visually compatible with the data, as an estimation of the uncertainty. Middle: Ratio of P- and S-wave spectrum. The colored part highlights the frequency range in which both P- and S-wave are above noise. Bottom: P- and S-wave spectra after correcting for source and attenuation. The dashed lines mark the expected values given the uncertainty in f_c . The curve is supposed to be flat until the pre-event noise level is reached (see top subplot).

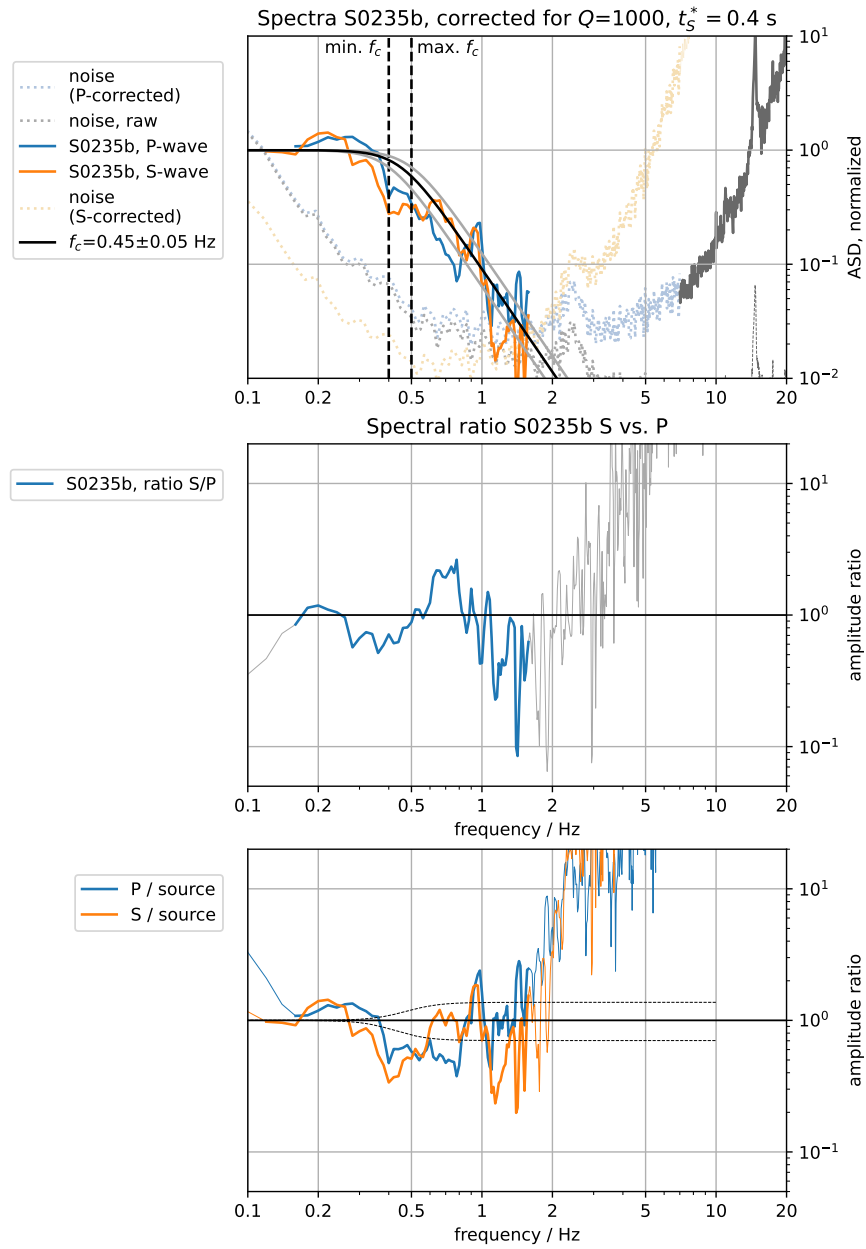


Figure 15: Event S0235b, after correction for Q_μ (eq. 5, 6). Plot is otherwise identical to 14

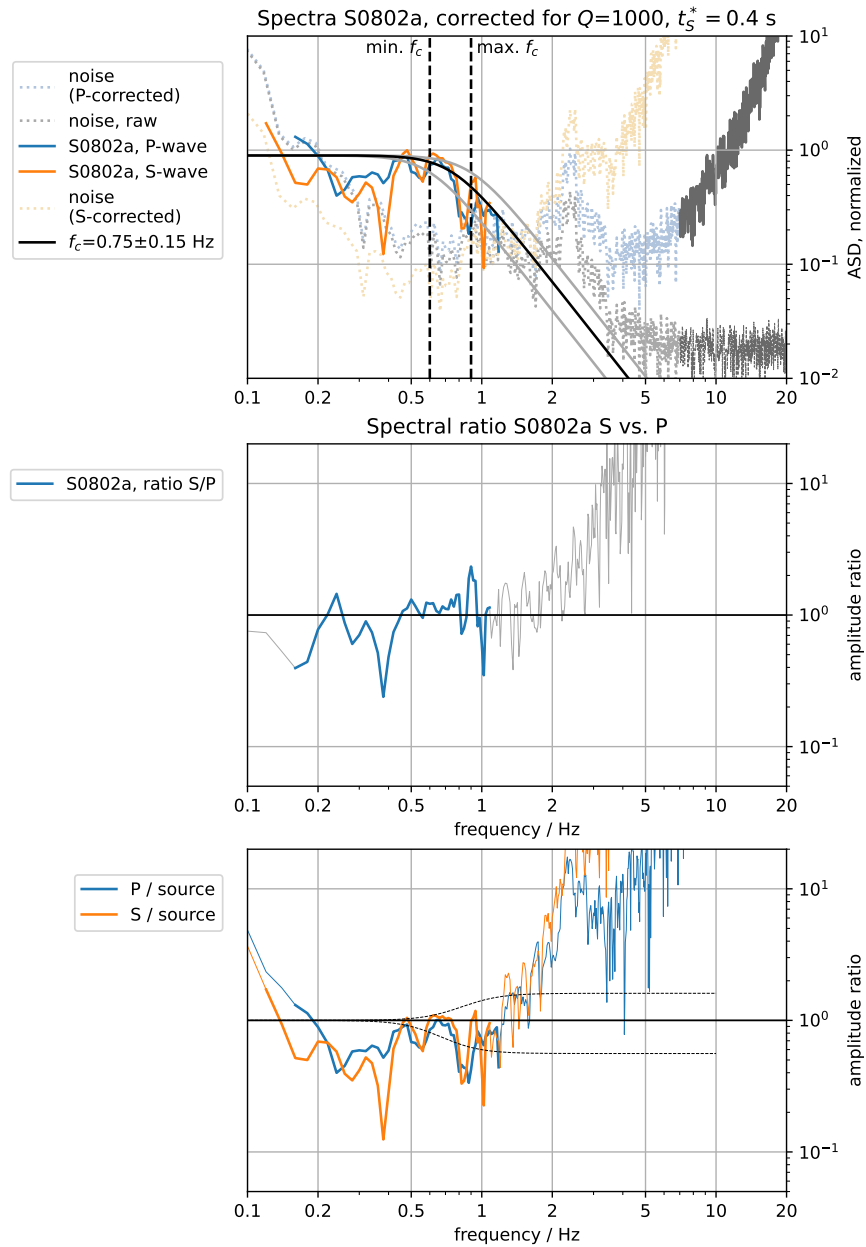


Figure 16: Event S0802a, after correction for Q_μ (eq. 5, 6). Plot is otherwise identical to 14

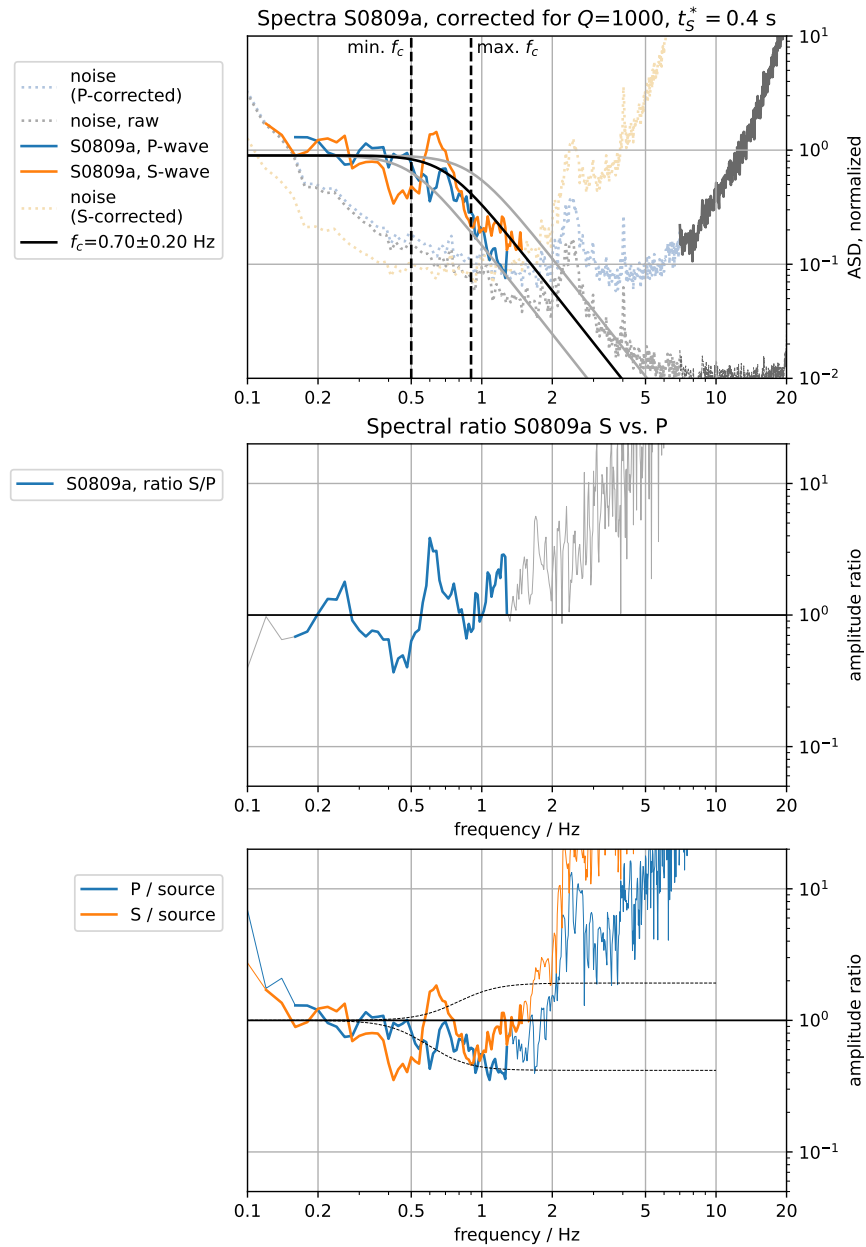


Figure 17: Event S0809a after correction for Q_μ (eq. 5, 6). Plot is otherwise identical to 14

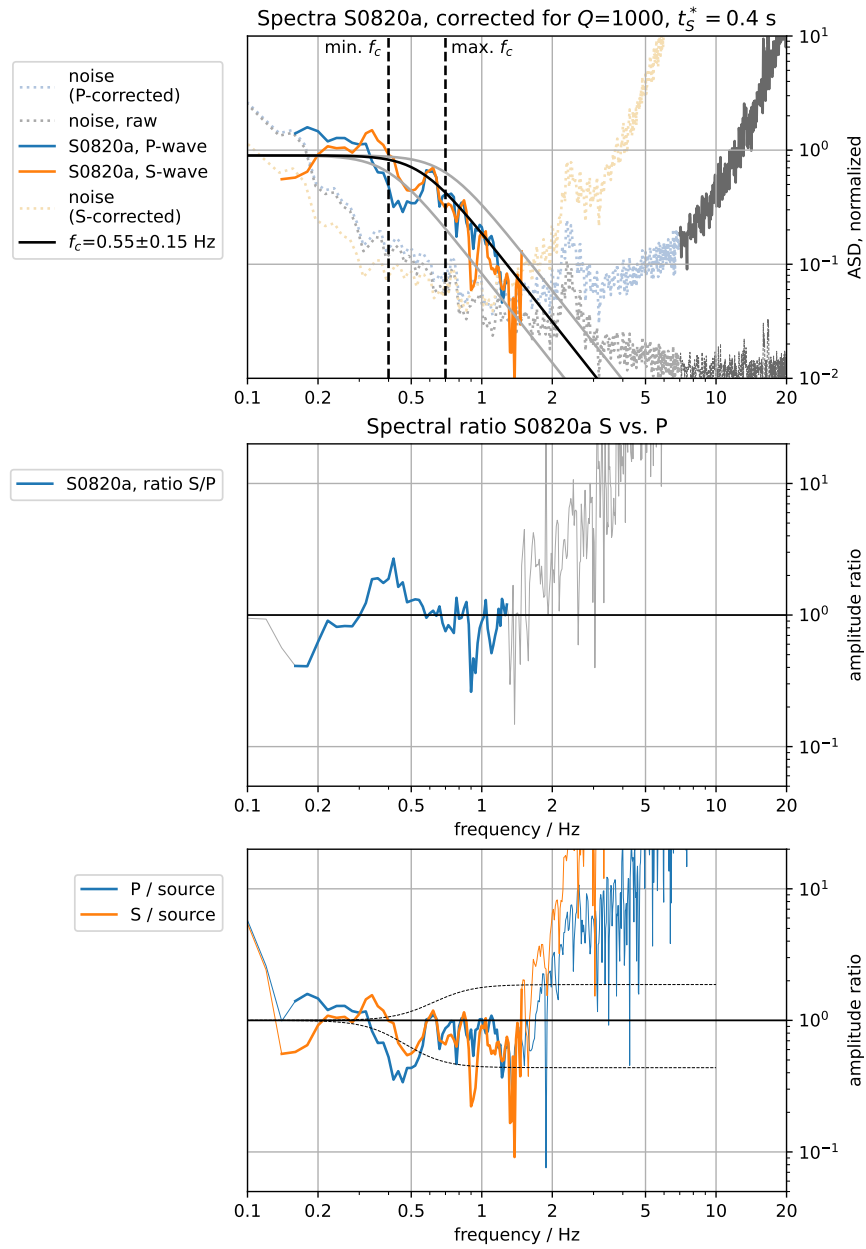


Figure 18: Event S0820a, after correction for Q_μ (eq. 5, 6). Plot is otherwise identical to 14

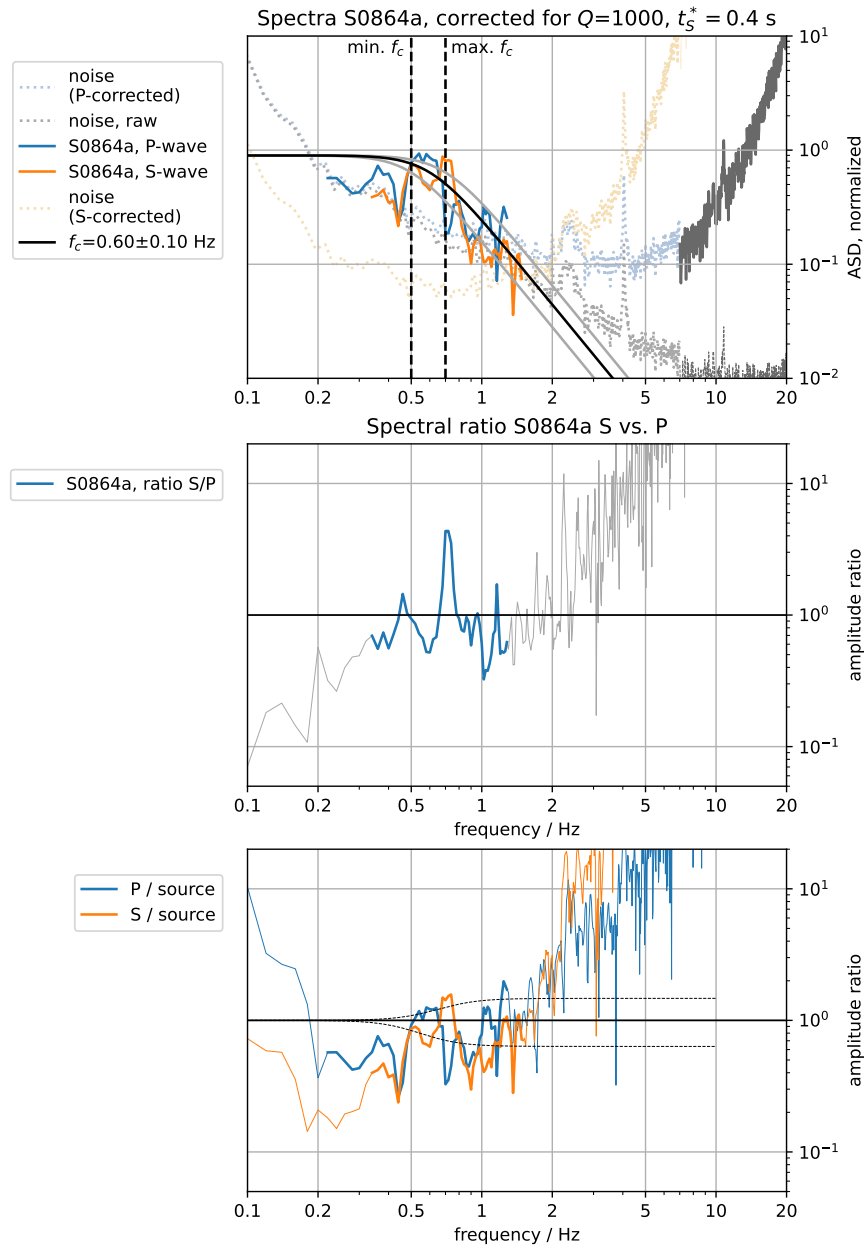


Figure 19: Event S0864a, after correction for Q_μ (eq. 5, 6). Plot is otherwise identical to 14

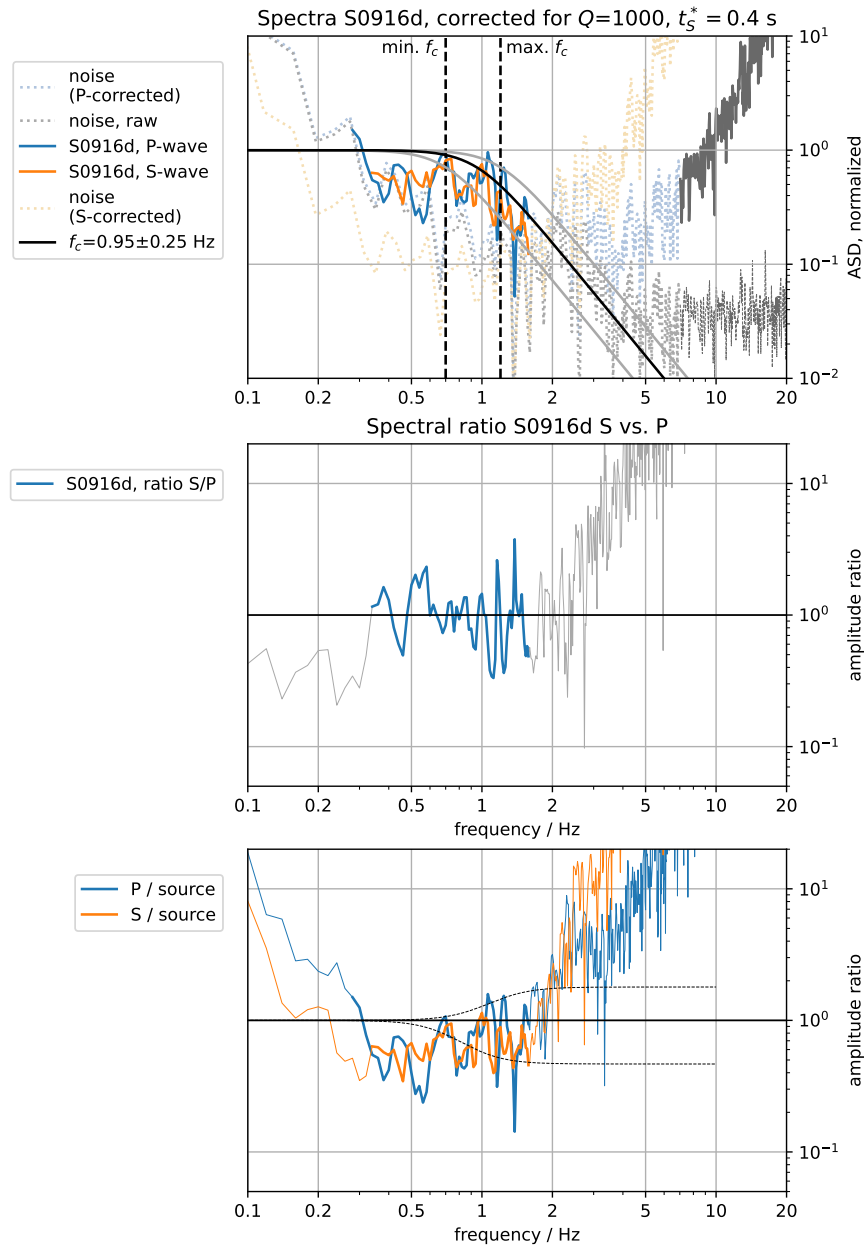


Figure 20: Event S0916d, after correction for Q_μ (eq. 5, 6). Plot is otherwise identical to 14

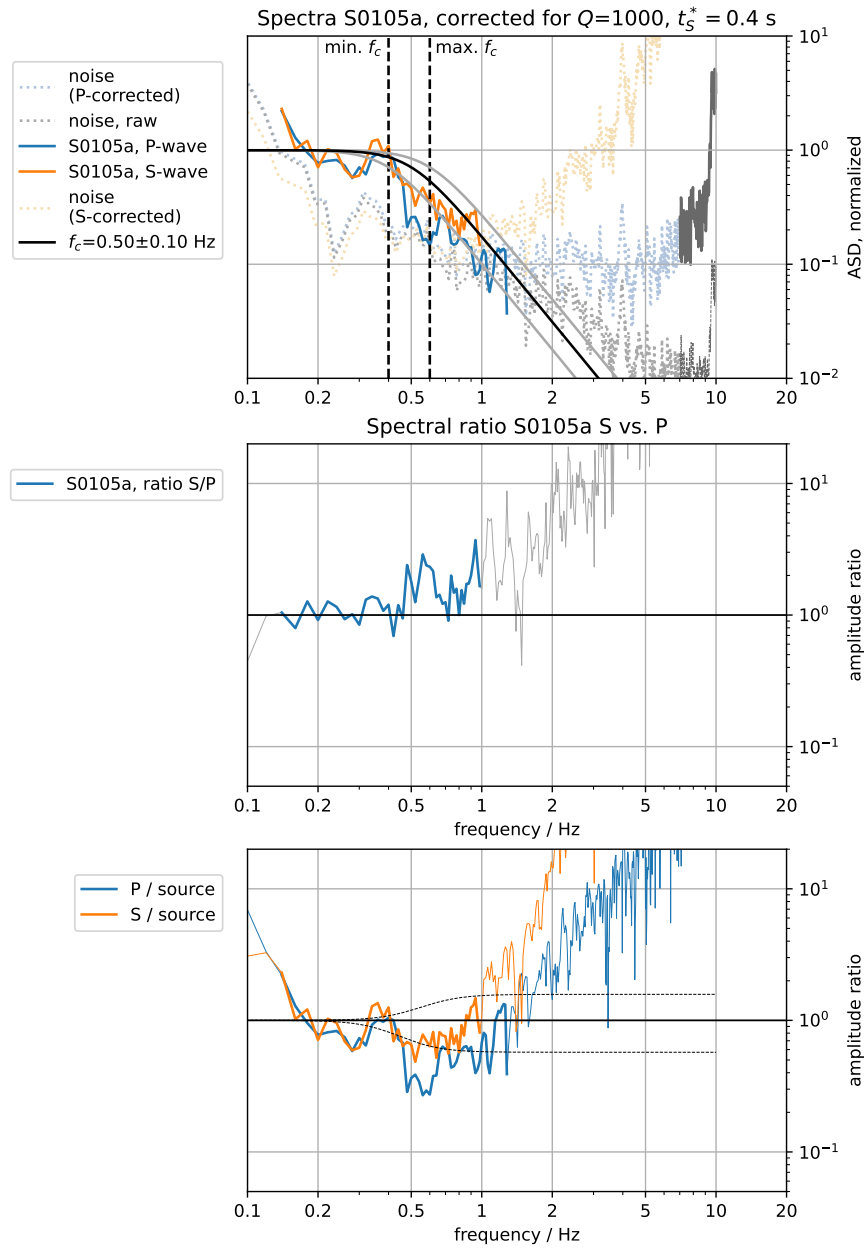


Figure 21: Event S0105a, after correction for Q_μ (eq. 5, 6). Plot is otherwise identical to 14

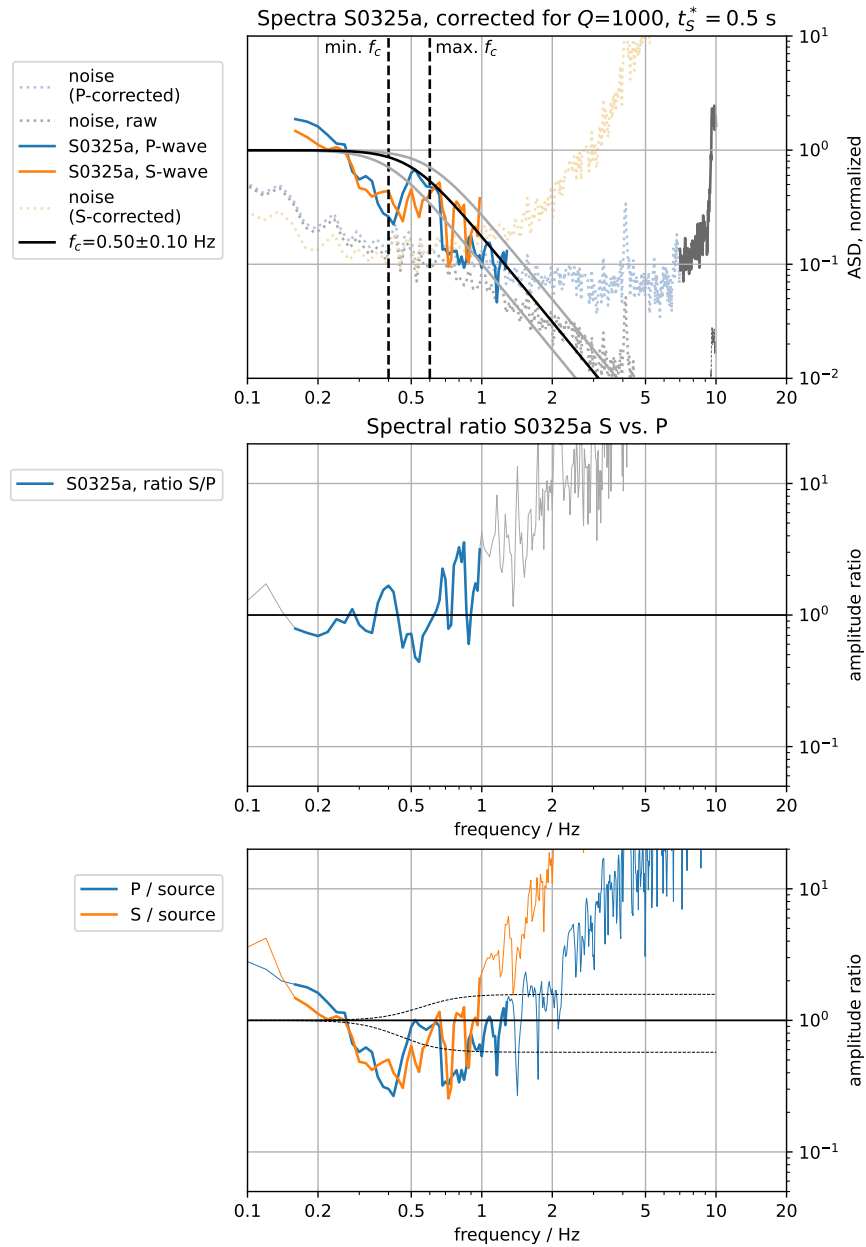


Figure 22: Event S0325a, after correction for Q_μ (eq. 5, 6). Plot is otherwise identical to 14

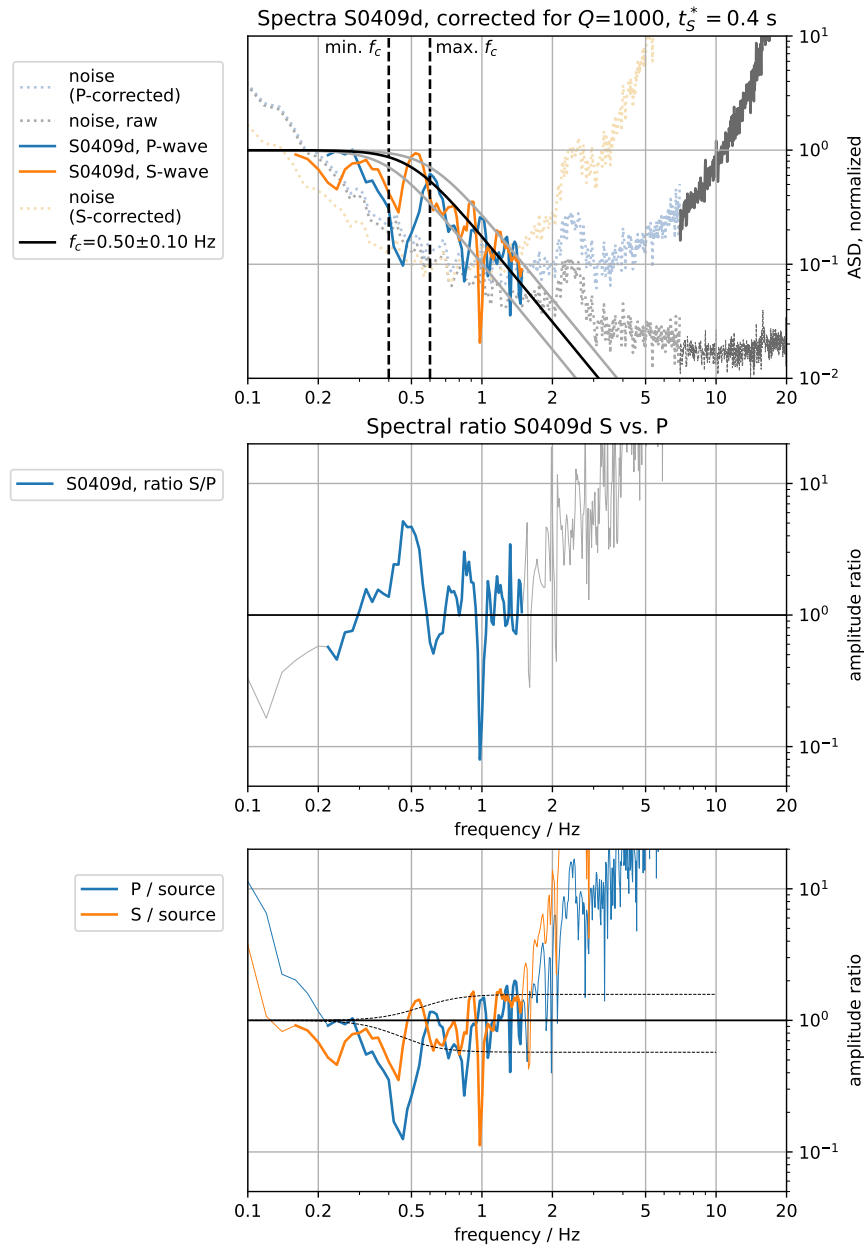


Figure 23: Event S0409d, after correction for Q_μ (eq. 5, 6). Plot is otherwise identical to 14

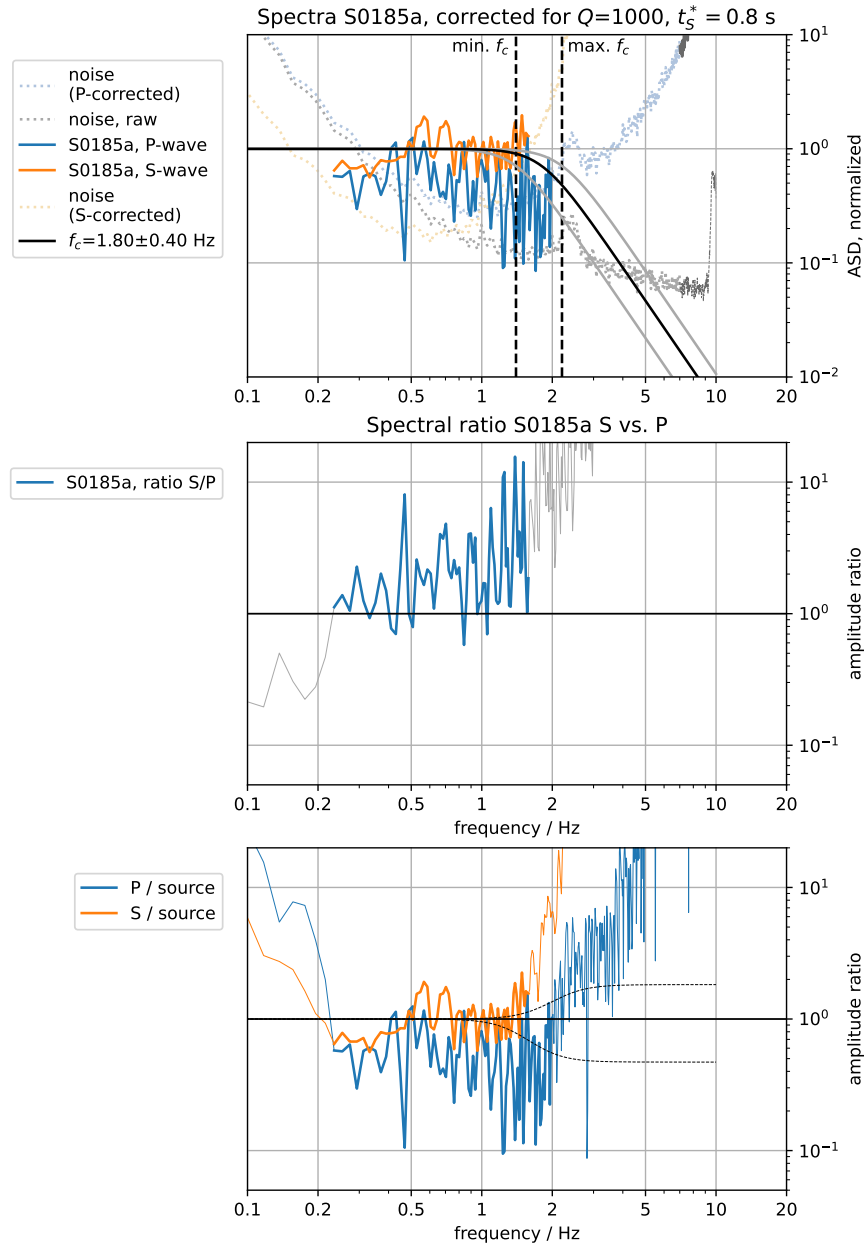


Figure 24: Event S0185aa, after correction for Q_μ (eq. 5, 6). Plot is otherwise identical to 14

546 **A.5.2 Events outside Cerberus Fossae**

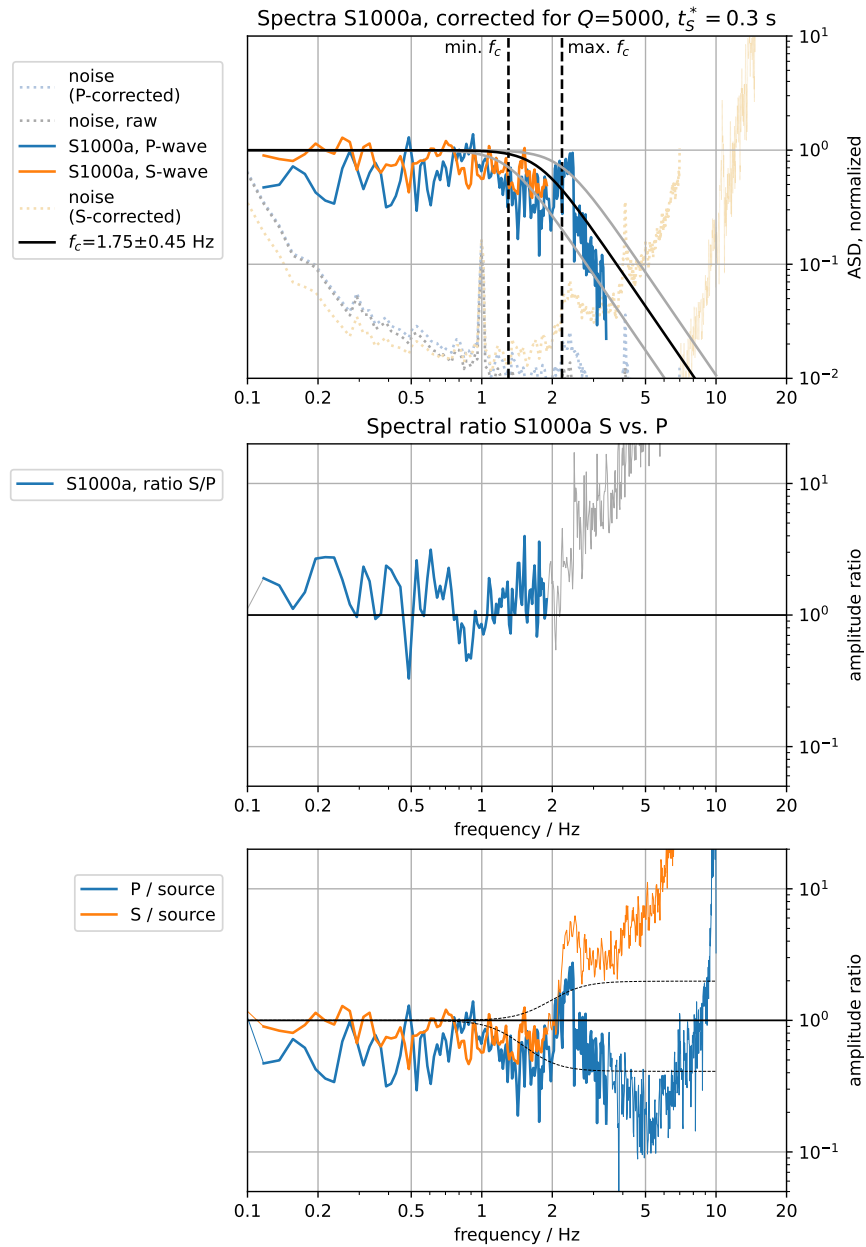


Figure 25: Event S1000a, after correction for Q_μ (eq. 5, 6). Plot is otherwise identical to 14

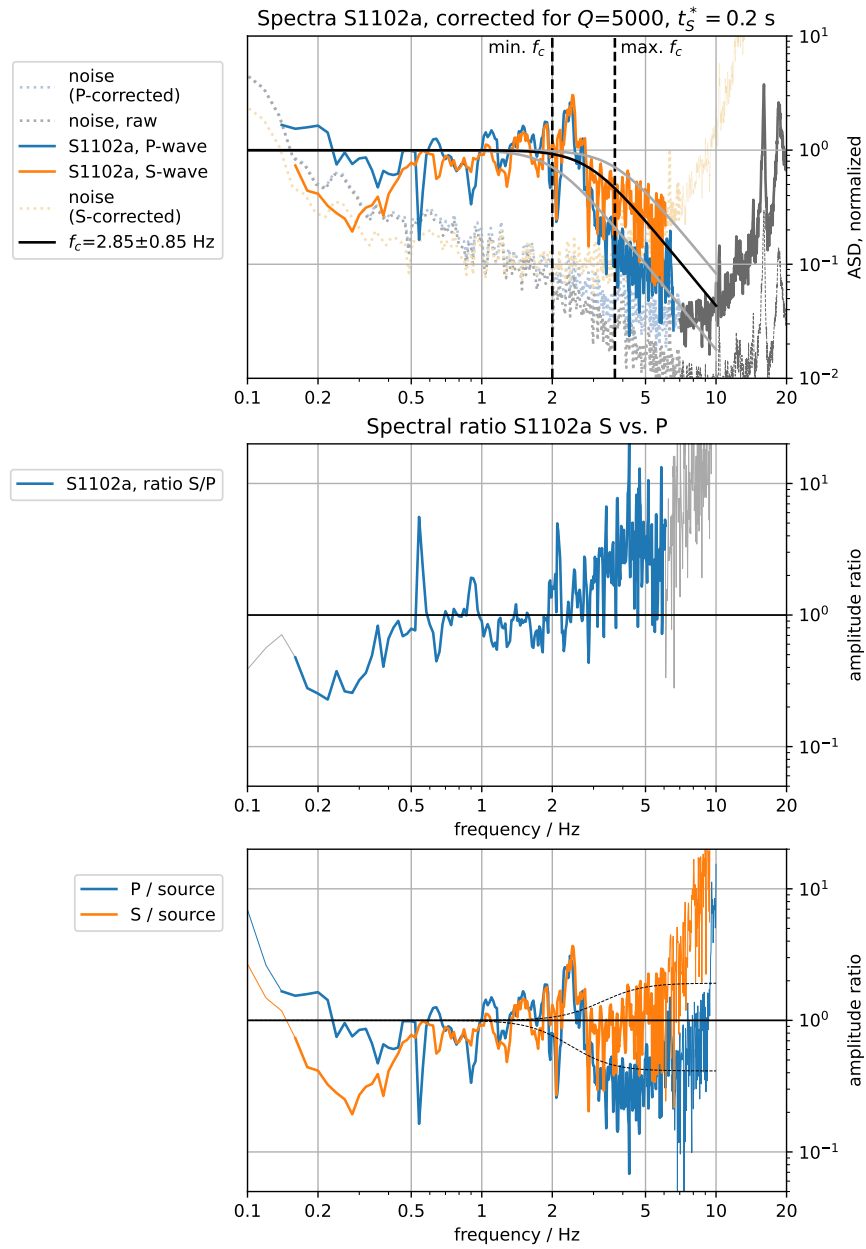


Figure 26: Event S1102a, after correction for Q_μ (eq. 5, 6). Plot is otherwise identical to 14